# PATZ1 Reinstates a Growth-Permissive Chromatin Landscape in Adult Corticospinal Neurons After Injury

Anisha S Menon[1,2], *Manojkumar Kumaran[1,]*,Deepta Susan Beji[1]*,Dhruva Kumar Kesireddy[1]**, Yogesh Sahu[1,2], Soupayan Banerjee[1], Sneha Manjunath[1], Katha Sanyal[1], Meghana Konda[1] and Ishwariya Venkatesh[1]

[1]Council of Scientific and Industrial Research (CSIR) – Center for Cellular and Molecular Biology (CCMB), Hyderabad, Telangana, India.

[2]Academy of Scientific and Innovative Research (AcSIR), Ghaziabad, Uttar Pradesh, India

*These authors contributed equally

Email Address: ishwariya@ccmb.res.in

**Acknowledgements**: This work was supported by grants from DBT, CSIR-CCMB, SERB-SRG, and CSIR (Awarded to Ishwariya Venkatesh)

**Conflict of Interest:** None

**Abstract**

As the CNS matures, chromatin at growth-associated genes gradually becomes less accessible, but the timing of this shift, the mechanisms behind it, and whether it can be reversed in adults have remained unclear. To address this, we mapped chromatin accessibility in corticospinal neurons across postnatal development and found two distinct waves of restriction—an early, partial closure between P0–P4, followed by a stronger, more widespread restriction from P7 into adulthood. We also asked whether the distance of injury influences chromatin remodeling and found that distal (thoracic) injuries triggered only modest changes, while proximal (intracortical) injuries led to much broader accessibility shifts, pointing to injury proximity as a key factor in epigenetic responsiveness. We then tested whether this restricted chromatin could be reopened by introducing PATZ1, a transcription factor normally expressed during early postnatal growth. AAV-based delivery of PATZ1 after injury caused marked chromatin remodeling, including an 11.6-fold increase in H3K27ac at growth-relevant sites and large-scale reorganization of 3D genome structure, with compartment shifts toward active states and altered TAD boundaries. These changes were accompanied by reactivation of gene networks linked to developmental growth. Our results help define when and how chromatin becomes restrictive in CNS neurons and show that it can be reopened using targeted interventions like PATZ1 to support regeneration.

## Introduction

Central nervous system (CNS) neurons largely fail to regenerate following injury, severely limiting recovery from traumatic brain injury, spinal cord injury, and neurodegenerative diseases(1–3). This regenerative failure stems from both a hostile external environment and internal constraints that develop as neurons mature (1, 2, 4–12). Among these internal limitations, the progressive restriction of chromatin accessibility around growth-associated genes represents a fundamental barrier to axon regrowth(13, 14). As neurons mature, the DNA regions controlling regenerative programs become increasingly compact and inaccessible to the cellular machinery needed for gene activation. While we have attempted to address this through broad-acting chromatin modifiers like histone deacetylase inhibitors, these approaches have shown limited success, likely due to their untargeted nature(14). There remains a critical need to develop precise approaches that remodel chromatin specifically at growth-relevant regions without disrupting essential neuronal functions.

Historically, studies on spinal cord injury have predominantly focused on transcription factor-mediated regulation of axon regeneration (4, 8, 15–18, 18–29); however, emerging evidence now highlights epigenetic regulation as a key additional layer of gene control (30–37), underscoring its importance in shaping regenerative competence. In zebrafish retinal neurons and mammalian sensory neurons, injury triggers selective chromatin relaxation around specific regulatory regions, allowing key transcription factors to bind DNA and activate regenerative programs(21, 24, 33, 38, 39). Recent work showed that peripheral nerve injury induces distinct patterns of histone modification and chromatin accessibility that correlate with successful regeneration, while central injuries fail to trigger similar epigenetic responses (38). Researchers have also demonstrated that disrupting chromatin organization impairs nerve regeneration in regeneration competent peripheral neurons (39). In contrast, we know surprisingly little about how chromatin becomes restricted in CNS neurons, when these changes occur during development, or whether this restriction can be manipulated. We also lack understanding of how injury distance affects chromatin reorganization in CNS neurons - knowledge that could inform new therapeutic strategies for promoting regeneration.

To fill these knowledge gaps, we mapped chromatin structure in cortical neurons across development and following spinal cord injury using several complementary techniques. We discovered that chromatin becomes restricted in two distinct waves during postnatal development (P0-P4 and P7-adulthood), and identified PATZ1 as a key transcription factor present during periods when neurons maintain growth potential. We found that neurons mount significantly stronger chromatin responses to nearby injuries than to distant ones, suggesting that injury proximity critically determines epigenetic plasticity. Most notably, delivering the PATZ1 gene to adult neurons substantially remodeled their

chromatin landscape after injury, increasing activation marks at growth-associated regions and reorganizing both local and higher-order chromatin structures. Our findings establish PATZ1 as a powerful regulator of chromatin architecture at regions controlling neuronal growth capacity, offering a new strategy for targeted chromatin remodeling that could enhance regenerative outcomes when combined with other pro-growth factors.

**Results:**

**Developmental Restriction of Chromatin Accessibility at Growth-Associated Regulatory Elements Occurs in Discrete Waves with Stage-Specific Transcription Factor Binding Patterns**

Our previous work demonstrated that cortical maturation progressively restricts chromatin accessibility at axon growth-associated genes, limiting both spontaneous regenerative capacity and the efficacy of pro-regenerative transcription factors in the adult CNS(13, 14). In contrast, regeneration-competent peripheral neurons successfully reactivate growth-supportive gene networks after injury by inducing chromatin relaxation at both promoters and distal enhancer regions(21, 38, 39). Understanding the precise epigenetic dynamics across development and injury in CNS neurons is therefore crucial, as these chromatin accessibility patterns appear to fundamentally control regenerative capacity and represent a key regulatory mechanism governing the neuron's intrinsic growth state.

However, several open questions remain regarding CNS neuronal chromatin dynamics: the precise developmental timing of chromatin restriction, whether enhancer regions undergo similar accessibility changes as promoters, and if the temporal dynamics of chromatin closure are synchronized between these regulatory elements. To address these knowledge gaps, we undertook a systematic analysis of chromatin accessibility dynamics at both promoters and enhancers across multiple developmental timepoints.

To map chromatin dynamics across development, we divided our analysis into pre- and post-natal periods. First, we examined whether neurons exhibit peak accessibility from their initial differentiation (E11-E12) or if key regulatory regions gradually become accessible over time, suggesting the involvement of specific factors in establishing chromatin accessibility patterns. To address this question, we leveraged open access ENCODE datasets spanning pre-embryonic ages through P0(40). Building upon our recent identification of enhancers regulating pro-growth genes during development, and using a curated list of pro-growth genes involved in developmental axon extension, we systematically mapped chromatin accessibility patterns around these critical regulatory regions throughout embryonic development (Figure 1A,B) (Table 1).

Our analysis of gene promoter accessibility across development revealed a striking pattern of

coordinated epigenetic regulation (Figure 1C, Table 1). We observed that genes associated with axon guidance, chromatin remodeling, cytoskeleton organization, DNA damage and repair, nervous system development, and regulation of cell growth initially displayed limited accessibility at early embryonic stages (E11-E12). Accessibility gradually increased during mid-embryonic development (E13-E14), reaching peak levels at late embryonic to early postnatal stages (E18-P0), coincident with periods of extensive axon growth and target innervation. Notably, this enhanced accessibility was transient, with a pronounced decline observed in adult neurons across all examined pathways. This temporal pattern suggests that rather than maintaining constitutive accessibility from neurogenesis, neurons undergo dynamic chromatin remodeling at growth-associated gene promoters, with accessibility precisely coordinated to match developmental needs.

To further characterize the developmental dynamics of chromatin accessibility, we extended our analysis to enhancer regions associated with the same functional pathways (Figure 1D, Table 1). Enhancers regulating genes involved in axon guidance, growth regulation, and cytoskeleton organization largely mirrored the temporal pattern observed at promoters—restricted accessibility in early embryonic stages (E11-E12), progressive opening during mid-development (E13-E18), peak accessibility around birth (P0), and subsequent restriction in adult neurons. However, we identified notable differences in pathway-specific enhancer regulation that diverged from promoter patterns. Enhancers associated with nervous system development maintained more sustained accessibility at P0, with a subset preserving open chromatin conformations into adulthood. Similarly, enhancers regulating chromatin remodeling genes displayed greater heterogeneity, with certain regions retaining accessibility in mature neurons. Most strikingly, DNA repair-associated enhancers exhibited a distinct pattern, with significantly higher retention of accessibility in adult neurons compared to their corresponding promoters. These findings reveal that while promoters undergo largely synchronous closing across pathways during maturation, enhancers display more nuanced, pathway-specific regulation. This differential regulation suggests that enhancer accessibility may provide an additional layer of control over gene expression potential that is more finely tuned to specific functional requirements in mature neurons.

Quantitative analysis of chromatin accessibility at both promoters and enhancers of pro-growth genes revealed striking developmental restriction patterns (Figure 1E-F, Table 1). Among the 291 pro-growth gene promoters examined, the vast majority (275 genes, 95%) displayed reduced accessibility in adult neurons compared to embryonic stages, while only 16 genes (5%) maintained accessibility into adulthood. Similarly, of the 1,228 known enhancer sites linked to pro-growth genes, 1,067 (87%) became restricted in adult neurons, while only 161 (13%) maintained accessibility. Further classification of restricted elements demonstrated a gradient of accessibility loss, with the largest category showing severe restriction (70-100% reduction): 140 promoters (51%) and 597 enhancers

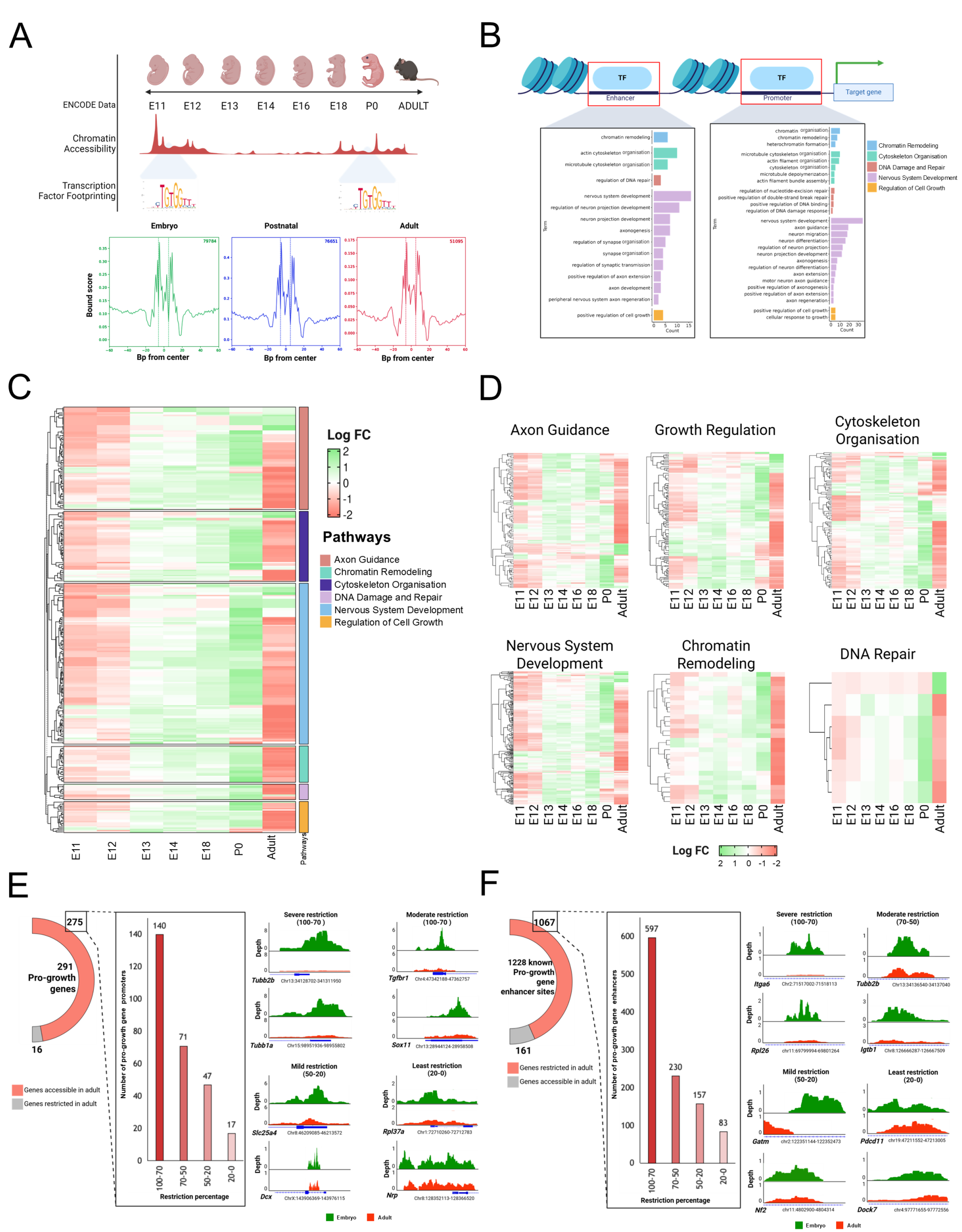


**Figure.1 ATAC-seq reveals severe restriction of promoter and enhancer accessibility in pro-growth genes across age** (A) Top panel: Schematic diagram of ENCODE ATAC-seq datasets isolated from the motor cortex of mice from early embryonic ages, Postnatal Day 0 (P0), and adult mouse cortex were analyzed for genome-wide patterns in chromatin accessibility. Bottom panel: Representative traces of transcription factor footprinting across age. (B) Pro-growth gene-specific promoters and enhancers were isolated for further analysis based on Gene Ontology (GO) Analysis. (p-value <0.05, Bonferroni correction, FDR <0.05). (C) Heatmap of promoter accessibility across ages, showing high accessibility at P0 (green) neurons and reduced accessibility in adults (red) (p-value <0.05, Bonferroni correction, FDR <0.05). (D)Heatmap of enhancer accessibility across age for growth-related GO terms. (p-value <0.05, Bonferroni correction, FDR <0.05). (E) UCSC genome browser examples of pro-growth gene promoters with varying degrees of restriction in adults (275 total; >50% show significant restriction). (F) UCSC genome browser examples of enhancer regions with varying levels of restriction in adults (1,067 total; most show >50% restriction).

(56%). The remaining regulatory regions showed varying degrees of restriction: moderate (50-70% reduction) in 71 promoters (26%) and 230 enhancers (22%), mild (20-50% reduction) in 47 promoters (17%) and 157 enhancers (15%), and minimal (0-20% reduction) in 17 promoters (6%) and 83 enhancers (8%). Representative ATAC-seq profiles from each category illustrate these distinct patterns of developmental chromatin dynamics. Notably, the proportion of enhancers that maintain some degree of accessibility in adult neurons (13%) is slightly higher than that observed for promoters (5%), suggesting that enhancer elements may retain marginally more regulatory potential in mature neurons. These findings demonstrate that developmental restriction of chromatin accessibility at pro-growth genes occurs along a spectrum and extends beyond promoters to include distal regulatory elements, with the majority of both promoters and enhancers becoming highly restricted and thus unavailable for transcriptional activation in adult neurons.

To investigate the temporal dynamics of chromatin accessibility restriction during postnatal development, we performed ATAC-seq on motor cortices isolated from mice at distinct developmental stages (P0, P4, P7, and adult) (Figure 2A). Analysis of promoter accessibility across these timepoints revealed a complex progression of chromatin remodeling (Figure 2B, Table 2). Most growth-associated gene promoters maintained relatively high accessibility from P0 through P7, followed by a pronounced restriction in adult neurons. However, this pattern varied across functional pathways, with some gene clusters in axon guidance and cytoskeleton organization beginning to show reduced accessibility at P4 and P7, while elements within nervous system development and chromatin remodeling pathways largely maintained accessibility through P7 before becoming restricted in adulthood.

When we extended our analysis to enhancer regions, we observed even more nuanced pathway-specific patterns (Figure 2D, Table 2). Axon guidance enhancers displayed heterogeneous dynamics, with some elements maintaining accessibility through P4 before restriction, while others showed earlier accessibility changes. Interestingly, a subset of growth regulation enhancers actually gained accessibility at P4 and P7 before becoming restricted in adult neurons. Cytoskeleton organization enhancers generally followed a more uniform progression toward restriction, though with varying degrees of residual accessibility in mature neurons. In contrast, enhancers associated with chromatin remodeling and DNA repair exhibited distinct behaviors, with subsets maintaining moderate accessibility even in adult neurons, suggesting differential regulation of these pathways into maturity.

To further quantify the extent of chromatin restriction during key developmental transitions, we directly compared accessibility changes between early postnatal (P0 vs P4) and late postnatal to adult (P7 vs Adult) periods (Figures 2C and 2E, Table 2). At promoter regions, we observed that 79.7% of pro-growth genes showed significant restriction between P0 and P4, while only 20.3% maintained accessibility (Figure 2C, top). Similarly, 64.3% of promoters became further restricted between P7 and

adulthood, with 35.7% retaining accessibility (Figure 2C, bottom). Categorizing these changes by restriction severity revealed a striking difference in the pattern between developmental stages. The P0-P4 transition predominantly affected promoters in the 20-50% restriction range, with very few sites experiencing severe (50-100%) restriction. In contrast, the P7-Adult transition showed a more uniform distribution across restriction categories, including substantial numbers of promoters undergoing severe restriction (Figure 2C, bar graph).

Similar analysis of enhancer elements revealed comparable overall restriction percentages between P0 and P4 (69.1% restricted, 30.9% accessible) but a slightly lower proportion restricted between P7 and adult stages (58.0% restricted, 42.0% accessible) compared to promoters (Figure 2E, top). However, the distribution across restriction categories showed distinctive patterns (Figure 2E, bottom). During the P0-P4 transition, enhancers predominantly exhibited mild to moderate restriction (0-50% ranges), with particularly high numbers in the 20-50% category. In contrast, the P7-Adult transition demonstrated a more even distribution, with substantial numbers of enhancers experiencing severe restriction (70-100%), which was rarely observed during the earlier transition.

To investigate the transcription factors (TFs) governing these chromatin dynamics, we performed ATAC-seq footprinting analysis at each developmental stage (Figure 2F, Table 2). Remarkably, we observed distinct stage-specific TF binding patterns at accessible chromatin regions. At P0, multiple neuronal growth factors from the nuclear receptor subfamily (NR2C1, NR2C2, NR2F1, NR2F6, NR4A1) and RAR-related factors (RARG, RARB) showed significant binding. By P4, the binding landscape began transitioning, with certain P0 factors diminishing while other TFs became more prominent. At P7, a distinct signature emerged dominated by SP1, SP2, and the zinc finger protein PATZ1, coinciding with the completion of most developmental growth programs. In adult neurons, binding patterns shifted dramatically toward BACH1, JUN, JUNB, FOXA1, JunB, JunD, and MEF2A - factors associated with mature neuronal function rather than growth.

Collectively, our analyses reveal that developmental chromatin restriction occurs in two major waves during postnatal development: an early wave (P0-P4) primarily involving partial restriction of many elements, and a later wave (P7-Adult) characterized by more severe restriction of remaining accessible regions. These changes in accessibility are accompanied by dynamic shifts in the TF binding landscape, with growth-promoting factors predominating in early development and maintenance-associated factors emerging in adulthood. The temporal dynamics identified P4 as a critical transition point, with substantial remodeling occurring between P0 and P4, followed by more subtle changes between P4 and P7, and then dramatic restriction between P7 and adulthood. These findings demonstrate that developmental chromatin restriction involves coordinated changes in both accessibility and TF binding patterns, occurring in discrete phases rather than as a continuous process,

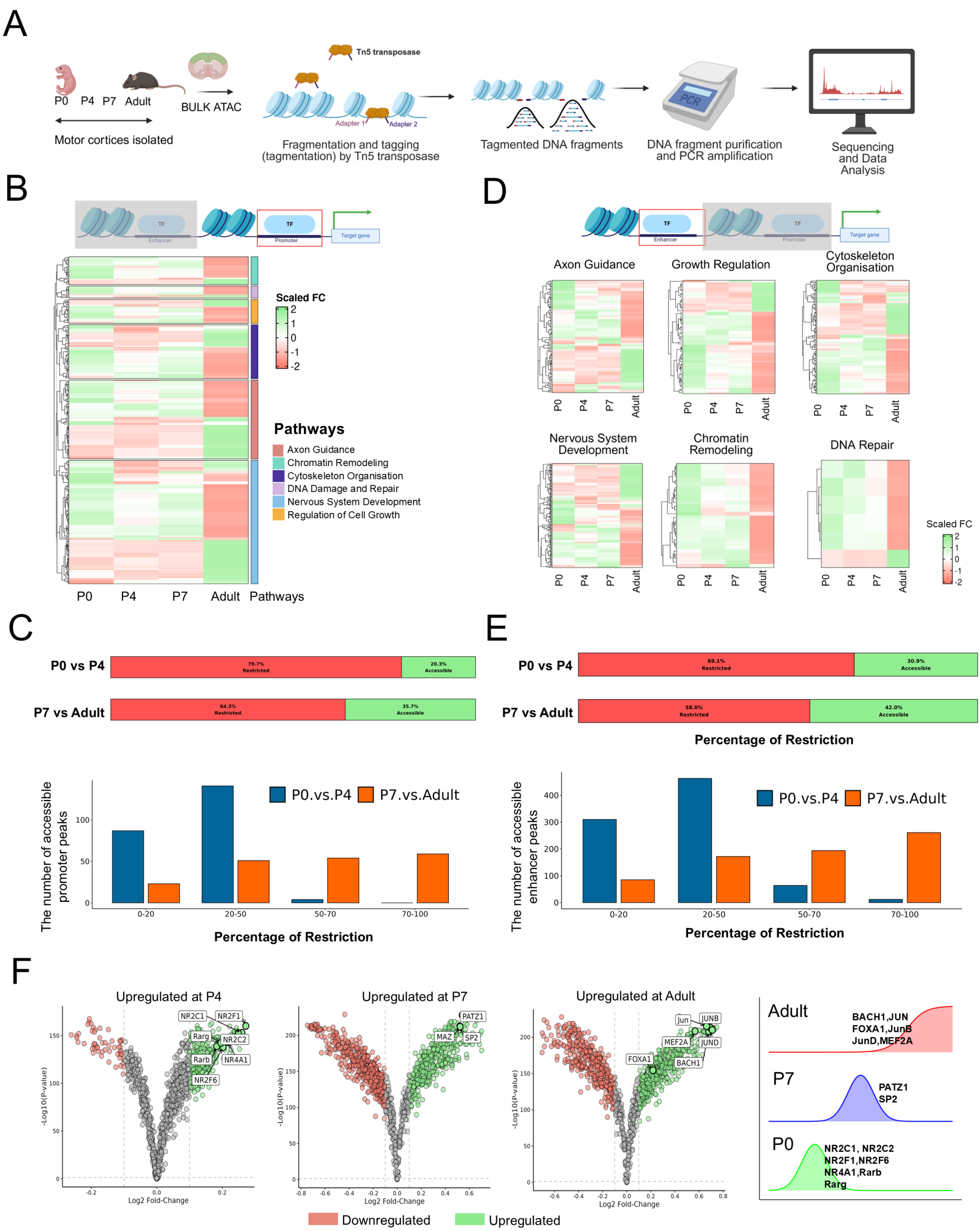


**Figure. 2 ATAC-seq reveals restriction of promoter and enhancer accessibility in pro-growth genes across post-natal stages** (A) Illustration of bulk ATAC sequencing procedure. (B) Heatmap of promoter accessibility across ages, showing high accessibility in postnatal day 0 (P0) neurons (green) and reduced accessibility from postnatal day 4 (P4) onwards (red) (p-value <0.05, Bonferroni correction, FDR <0.05). (C) Top panel: Comparative analysis of pro-growth gene promoter accessibility showing dynamic regulation across development: P0 vs P4 (36.7% accessible, 63.3% restricted) and P7 vs Adult (26.3% accessible, 73.7% restricted). Bottom panel: Distribution of promoter restriction levels showing progressive increase in restriction from early postnatal stages to adult stage (>70%). (D) Heatmap of enhancer accessibility across ages for growth-related GO terms (p-value <0.05, Bonferroni correction, FDR <0.05). (E) Top panel: Comparative analysis of pro-growth gene enhancer accessibility showing dynamic regulation across development: P0 vs P4 (30.9% accessible, 69.1% restricted) and P7 vs Adult (42% accessible, 58% restricted). Bottom panel: Histogram quantification of enhancer restriction levels across developmental stages, demonstrating a shift from lower restriction (0-50%) in early postnatal comparisons to higher restriction (>50%) in P7 vs Adult comparison. (F) Volcano plots showing stage-specific transcription factor expression. Left plots show differential expression at P4 (NR2C1, NR2F1, NR2C2, NR4A1, RARB, RARG), P7 (PATZ1, SP2), and Adult stages (BACH1, JUN, JUNB, JUND, FOXA1, MEF2A). Right panel illustrates the differential transcription factors present in P0, P7 and Adult

with the most pronounced changes coinciding with the completion of major developmental growth programs. The end result is a highly restricted chromatin landscape in adult neurons, with the vast majority of growth-associated genes becoming inaccessible to transcriptional machinery or bound by non-growth-promoting factors, potentially contributing to their limited regenerative capacity.

**Thoracic Spinal Cord Injury Induces modest but Pathway-Specific Chromatin Accessibility Changes in Corticospinal Neurons**

Next we wanted to look into the dynamics of chromatin accessibility following spinal injuries. Although we have detailed maps of how regeneration-competent neurons like peripheral neurons and zebrafish retinal ganglion cells respond to injury in terms of relaxation of chromatin(21, 38, 39), similar maps for CNS neurons is absent. It is unknown whether they respond with any relaxation around growth-relevant loci or none at all. To address this, we performed thoracic crush injuries in mice, and seven days later collected their motor cortices, FACS sorted their nuclei and carried out single-nucleus ATAC-Seq to get profiles of chromatin accessibility in response to injury (Figure 3A, Table 3). We successfully profiled 1,320 nuclei from injured animals and 2,031 nuclei from uninjured controls, all confirmed as CST neurons based on established Layer 5 excitatory neuron (L5ET) marker gene expression patterns like *Satb2, Lrp8, Etv1, Tnnc1, Crym, and Mrpl11(6).*

Following differential accessibility analysis of ATAC-seq data from injured versus uninjured corticospinal neurons, we identified a moderate but clear chromatin response to injury (Figure 3C-D,Table 3). Specifically, we detected 5,482 genomic regions with increased accessibility (upregulated peaks) and 6,000 regions with decreased accessibility (downregulated peaks) in injured neurons. Annotation of these differential peaks revealed that the majority (74.4%) corresponded to potential enhancer regions, while 25.6% mapped to promoters (Figure 3C, pie chart). Analysis of the magnitude of accessibility changes showed that most differential peaks exhibited moderate log2 fold changes between 1.5-2.5 (Figure 3C, histogram). Gene ontology (GO) analysis of the differentially accessible regions revealed significant enrichment for terms related to transcriptional regulation, signal transduction, and cell differentiation (Figure 3D, left). Most notably, when examining the proportion of injury-specific peaks across different functional pathways, we observed that DNA damage (60.6%), regulation of cell growth (59.4%), cytoskeleton organization (53.3%), and chromatin remodeling (53%) exhibited the highest percentages of unique injury-induced peaks (Figure 3D, right). This suggests that while overall chromatin changes are limited compared to peripheral neurons, corticospinal neurons do mount a focused chromatin response targeting specific cellular processes after injury.

To further characterize the injury-induced chromatin response, we examined the fold-change distribution and pathway-specific patterns of differential accessibility (Figure 3E-G, Table 3). Radar plot analysis revealed pathway-specific differences in the magnitude of chromatin changes following injury (Figure 3E). Regulation of cell growth showed the highest number of differential peaks (402),

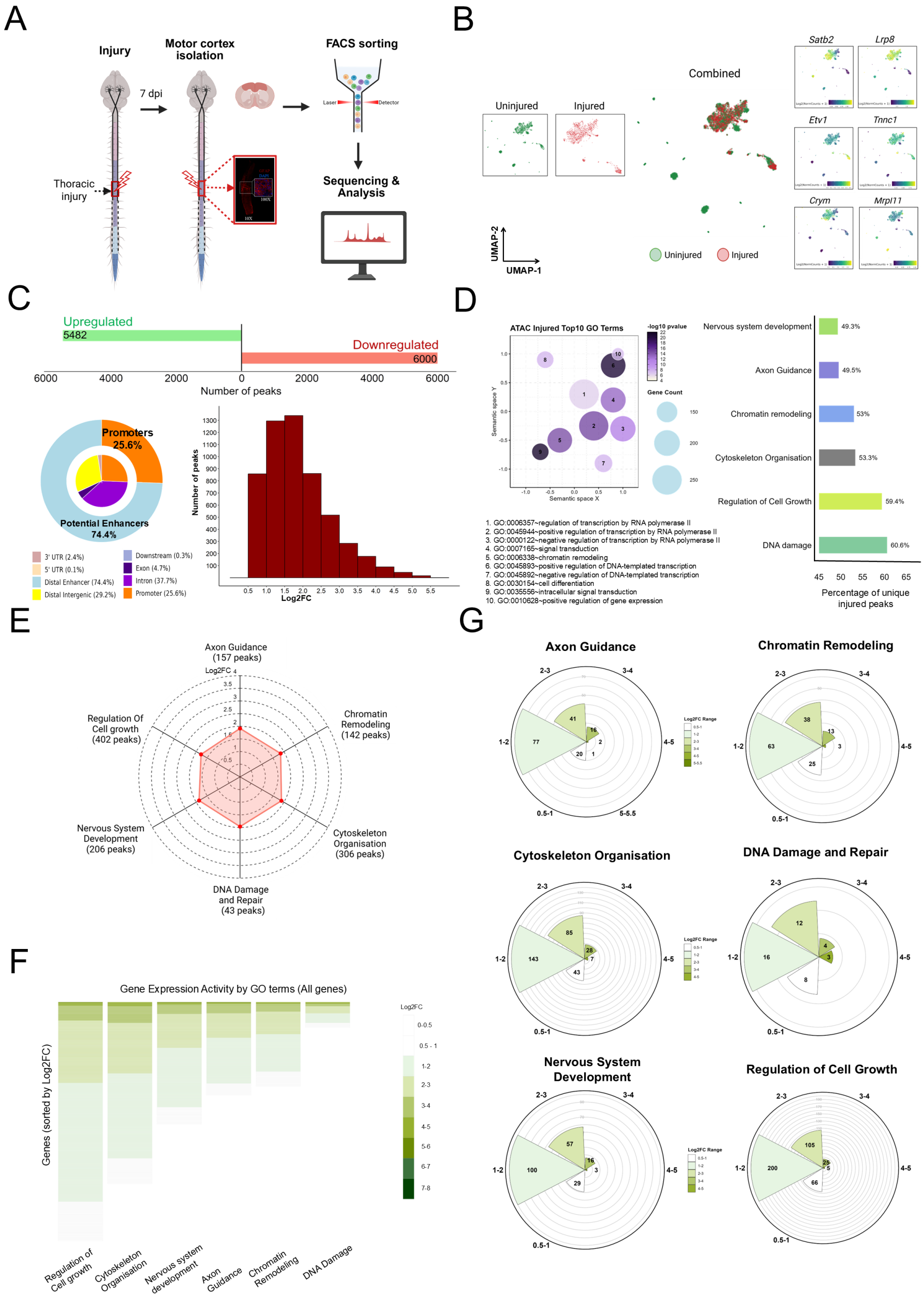


**Figure.3 Single-nuclear (sn)ATAC-seq reveals that CNS neurons mildly open the chromatin post-injury at key loci** (A) Schematic representation of single-nucleus ATAC-seq (snATAC) experimental workflow. (B) Uniform Manifold Approximation and Projection (UMAP) dimensional reduction plot showing single-nucleus ATAC-seq clustering. The plot displays three conditions: Uninjured (control, green), Injured (red), and Merged (combined clusters, mixed colours), along with the marker genes *Satb2, Lrp8, Etv1, Tnn1, Crym, Mrp11* marking the L5 ET clusters. (C) The bar graph (top) represents the number of chromatin accessibility peaks identified as significantly upregulated (green) and downregulated (red) post-injury in snATAC-seq analysis. The pie chart (bottom left) illustrates the genomic distribution of the upregulated peaks, with 74.4% located in potential enhancer regions and 25.6% in promoters. The histogram (bottom right) depicts the log2 fold-change distribution of upregulated peaks, with the majority exhibiting moderate fold changes. (D) Left panel bubble-plot shows clustered GO terms in two-dimensional semantic space, with circle size representing gene count and colour intensity indicating statistical significance (-log10 p-value). Right panel displays the percentage of unique injured peaks associated with key biological processes. (E) Radar chart comparing the magnitude and distribution of chromatin accessibility changes injured (red) neurons across six key biological pathways.The concentric circles represent Log2FC values ranging from 0.5 to 4.0. (F) Heatmap showing gene expression activity across key biological pathways as determined by GO term analysis. The vertical axis represents genes sorted by Log2FC values while the horizontal axis displays the six major pathways. Colour intensity corresponds to Log2FC values according to the scale bar (right), with darker green indicating higher accessibility. (p-value <0.05, Bonferroni correction). (G) Circular-bar plots showing the distribution of chromatin accessibility peaks based on their Log2 fold change (Log2FC) magnitudes across six key biological pathways. Each plot displays the angular position representing the magnitude of fold change (ranging from 0.5 to 5.5), which is also signified by the intensity of green shading. The radial bars indicate the number of differential accessibility peaks at each fold change value for the pathways.

followed by cytoskeleton organization (306), nervous system development (206), and axon guidance (157), while DNA damage and repair exhibited the fewest changes (43 peaks). The heatmap of gene expression activity organized by GO terms (Figure 3F, Table 3) demonstrated modest but consistent upregulation across these pathways, with regulation of cell growth showing the strongest response. Detailed circular plots of each pathway (Figure 3G) revealed distinct patterns in the distribution and magnitude of accessibility changes. For cytoskeleton organization and regulation of cell growth, a substantial proportion of peaks showed moderate fold changes (1-2 log2FC range), with 143 and 200 peaks respectively. In contrast, axon guidance and chromatin remodeling pathways showed more balanced distributions across fold-change categories. DNA damage and repair, despite having fewer total differential peaks, showed a higher proportion of strongly upregulated regions (>3 log2FC). Collectively, these findings demonstrate that while injury-induced chromatin accessibility changes in corticospinal neurons are considerably more limited than those observed in peripheral neurons, they do exhibit pathway-specific responses that appear targeted toward cellular repair processes rather than axon regeneration programs.

This represents the first detailed characterization of how CST neurons respond to injury in terms of chromatin accessibility. Although transcriptionally researchers have observed minimal responses to a thoracic injury(6), it does seem that epigenetically some response is mounted albeit insufficient to translate to robust transcriptional activation of growth-promoting programs.

**Proximity to Injury Site Enhances Chromatin Accessibility in Corticospinal tract Neurons**

Recently it was revealed that the injury distance affects the transcriptional activation in response to injury(6). We wanted to test if similarly injury distance plays a role in the epigenetic remodeling in response to injury as well. To investigate this question, we compared chromatin accessibility changes following intra-cortical injury (ICI) versus thoracic crush injury (TCI) in corticospinal neurons (Figure 4). Our ATAC-seq analysis revealed a significant difference in the magnitude of chromatin response based on injury proximity. Intra-cortical injuries induced substantially more accessibility changes (13,084 peaks) compared to thoracic injuries (1,390 peaks), representing nearly a ten-fold difference (Figure 4B, Table 4). The genomic distribution of these accessible regions was similar between injury models, with the majority mapping to potential enhancer regions (78.2%) and the remainder to promoters (21.8%). Examination of fold-change distributions further emphasized this disparity, with ICI samples showing a robust response peaking at 80-85% fold change, while TCI samples exhibited limited changes across all fold-change categories (Figure 4C, Table 4).

Gene ontology analysis revealed that ICI-specific accessible regions were significantly enriched for neuronal processes, transcriptional regulation, and growth-associated pathways compared to TCI (Figure 4D, Table 4). This pattern was consistent across all analyzed neurobiological pathways, with axon guidance (411 vs. 36 peaks), chromatin remodeling (394 vs. 51), cytoskeleton organization (296 vs. 40), nervous system development (619 vs. 49), and regulation of cell growth (1,669 vs. 103) showing considerably higher accessibility in ICI versus TCI (Figure 4E, left). Gene-specific analyses

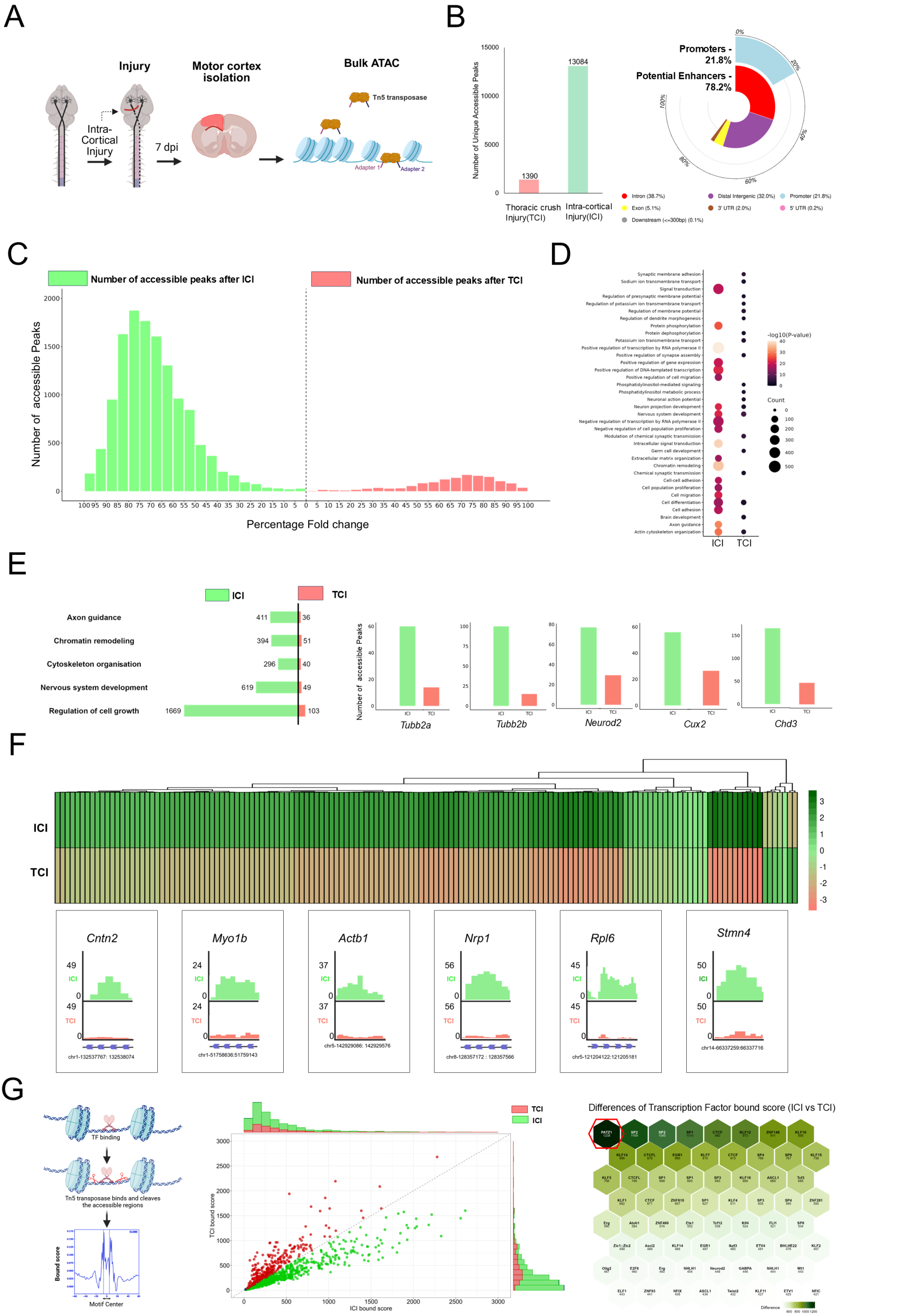


**Figure.4 ATAC-seq reveals injury site proximity affects the re-opening of key loci six-fold** (A) Experimental workflow for ATAC-seq profiling after Intra-cortical Injury (ICI). (B) Quantification of accessible chromatin regions. Bar graph comparesThoracic crush injury (TCI) (1,390 peaks) versus ICI (13,084 peaks). Pie chart shows genomic distribution with enhancers (78.2%) and promoters (21.8%). (C) Distribution of accessible peaks by percentage fold change between injury models. ICI samples (green) show higher peak numbers with a maximum of 80-85% fold change compared to TCI samples (red). (D) Gene ontology (GO) analysis of differentially accessible regions. Dot plot shows enriched pathways with color indicating significance (-log10(P-value)) and size showing gene count. ICI samples show greater enrichment in neuronal processes compared to TCI. (E) Pathway and gene-specific accessibility comparison. Left: Key neurobiological pathways show consistently higher accessibility in ICI versus TCI. Right: Neuronal genes (*Tubb2a, Tubb2b, Neurod2, Cux2, Chd3*) display greater accessibility in ICI than in TCI. (F) Pro-growth gene accessibility profiles. Top: Heatmap showing clustering of accessibility (green = increased). Bottom: UCSC browser tracks of six representative pro-growth genes showing higher accessibility peaks in ICI (green) versus TCI (red). (p-value <0.05, Bonferroni correction, FDR <0.05). (G) Left: Schematic illustration of TF footprinting analysis showing TF binding to DNA and Tn5 transposase cleavage of accessible regions, resulting in characteristic footprint patterns. Center: Scatter plot comparing IC bound scores (x-axis) vs TC bound scores (y-axis) with marginal histograms, demonstrating differential TF binding between injury conditions. Right: Hexplot visualisation of the differences in transcription factor binding scores between ICI and TCI conditions. The colour intensity (light to dark green) represents the magnitude of difference, with the darkest hexagons (e.g., PATZ1, SP2) indicating transcription factors with the greatest differential binding between conditions.

of neuronal markers including *Tubb2a, Tubb2b, Neurod2, Cux2*, and *Chd3* confirmed this pattern (Figure 4E, right). Detailed examination of pro-growth gene loci revealed divergent accessibility profiles between injury models (Figure 4F, Table 4), with key genes such as *Cntn2, Myo1b, Actb1, Nrp1, Rpl6*, and *Stmn4* showing substantial accessibility in ICI but minimal accessibility in TCI samples. Transcription factor footprinting analysis further demonstrated distinct binding patterns between injury conditions (Figure 4G, Table 4), with transcription factors including PATZ1, SP2, SP3, SP1, and KLF family members showing significantly higher binding scores in ICI compared to TCI. Collectively, these findings demonstrate that injury proximity serves as a critical determinant of epigenetic remodeling capacity in CNS neurons, with proximal injuries triggering extensive chromatin accessibility changes that enable transcriptional activation of growth-associated programs, while distal injuries elicit only limited epigenetic responses.

**PATZ1 Binding hints Age-Dependent Regulation of Chromatin Accessibility in Pro-Growth Regions**

We were surprised to see strong binding of PATZ1 to differentially accessible regions in the ICI, as it is relatively unknown in the context of axon growth regulation. Recent work has characterized PATZ1 as a member of the "stripe" transcription factor superfamily that recognizes overlapping GC-rich sequences in mammalian genomes (41). This superfamily, which includes members of the SP, KLF, EGR, and ZBTB families, has been shown to provide chromatin accessibility to co-binding partners through their recognition of GC-rich motifs. Stripe factors like PATZ1 help establish open chromatin regions, facilitate the recruitment of other transcription factors, and increase their residence time at regulatory elements, ultimately supporting proper gene expression (41). Given this established role in modulating chromatin accessibility, we hypothesized that PATZ1 may be playing a similar function in regulating chromatin dynamics in CNS neurons across development and after injury.

To investigate PATZ1's potential role in neural chromatin regulation, we analysed its binding patterns across developmental stages using ATAC-seq footprinting (Figure 5A). Our analysis revealed a distinct pattern where PATZ1 binding was high in regeneration-competent embryonic and postnatal neurons but significantly decreased in adult neurons. This age-dependent decline in PATZ1 binding parallels the progressive restriction of chromatin accessibility and regenerative capacity observed during CNS maturation. Quantification of transcription factor footprints across developmental stages (Figure 5B, Table 5) showed that PATZ1 ranked highest among all transcription factors in young neurons, suggesting its role as a broad chromatin regulator during early development. The heatmap in Figure 5B further illustrates how PATZ1 and other stripe factors (including ZNF148, SP1/2/3, and KLF family members) show robust binding in embryonic and postnatal stages, with substantially reduced accessibility in adult neurons.

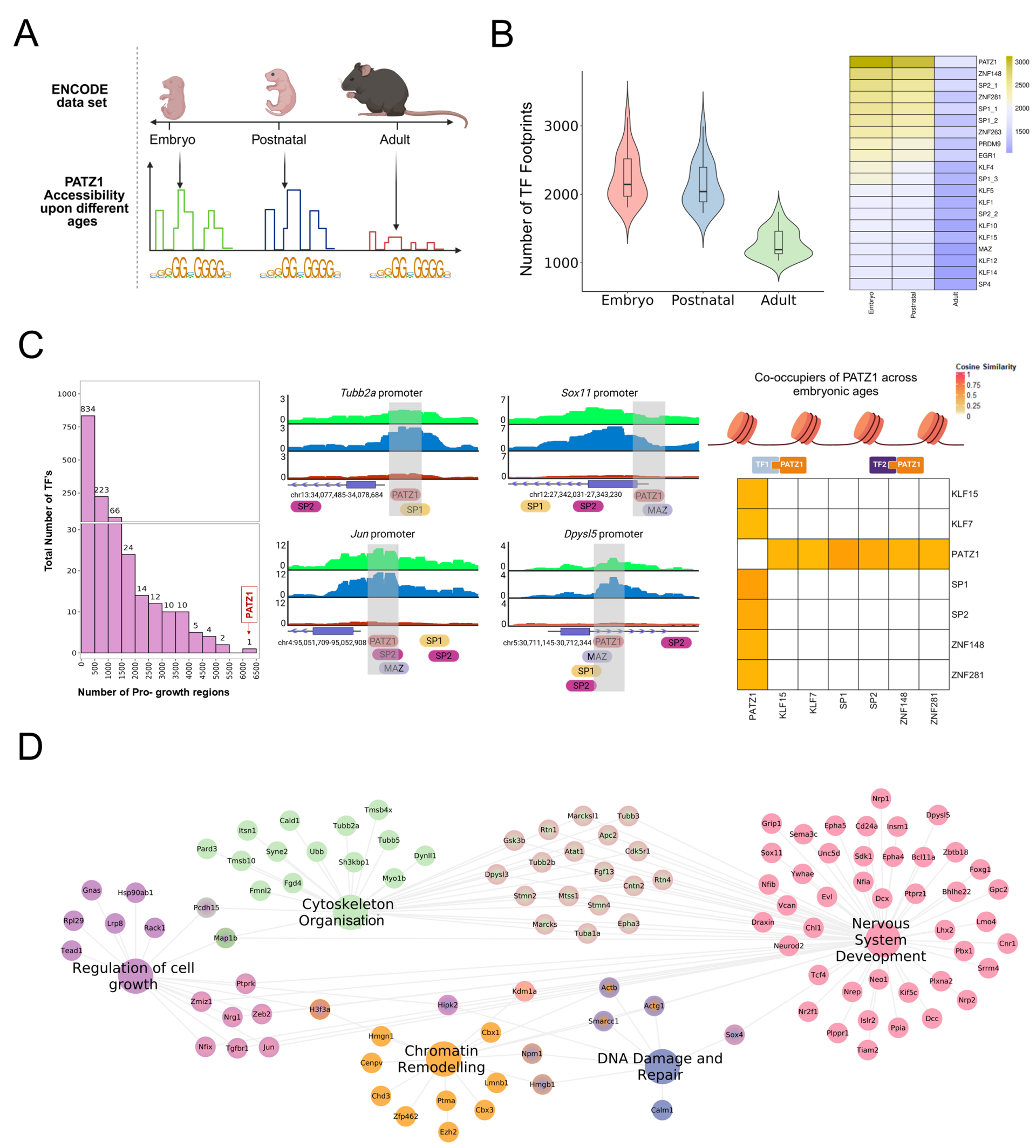


**Figure. 5 PATZ1-mediates transcriptional regulation of pro-growth genes during development**. (A) Illustration of transcription factor footprinting analysis methodology. (B) Left panel: Violin plots depicting the distribution of transcription factor footprints across embryonic, postnatal, and adult stages, demonstrating progressive reduction in transcription factor (TF) binding sites in adult. Right panel: Heatmap of key transcription factor footprinting across developmental stages (embryo, postnatal, adult), where colour intensity indicates footprint count (lighter colours represent a higher number of footprints). (C) Left panel: Distribution histogram showing PATZ1 binding frequency across pro-growth target regions. Middle panel: Representative genome browser tracks displaying PATZ1 co-occupancy with transcription factors (SP1, SP2, MAZ) at selected promoters (*Tubb2a, Sox1, Jun*, and *Dpysl5*). Right panel: Top - Schematic illustration of PATZ1 co-binding patterns; Bottom - Heatmap showing cosine similarity scores of PATZ1 co-occupiers across embryonic ages, highlighting six major co-binding transcription factors (KLF7, KLF15, SP1, SP2, ZNF148, and ZNF281).
(D) Network analysis of PATZ1-bound pro-growth target genes grouped into five major functional clusters: regulation of cell growth (purple), cytoskeleton organisation (green), chromatin remodeling (orange), DNA damage and repair (blue), and nervous system development (pink). Nodes represent individual genes, and edges indicate functional connections between genes.

When we focused specifically on pro-growth genomic regions, PATZ1 emerged as the most widely bound factor in young neurons, with clear footprints at key growth-associated genes including *Tubb2a, Sox11, Jun*, and *Dpysl5* (Figure 5C). Quantitative analysis revealed that PATZ1 bound to over 800 pro-growth regions in embryonic neurons, with progressively fewer binding sites in postnatal and adult stages (Figure 5C, left panel). This selective binding to growth-associated loci suggests that PATZ1 may play a specific role in regulating the accessibility of regeneration-associated genes during development (Table 5). The browser tracks in Figure 5C demonstrate how PATZ1 footprints (highlighted in gray) overlap with other stripe factors at prominent growth-associated gene promoters, with strong signal in embryonic (green) and postnatal (blue) stages, but minimal binding in adult neurons (red).

Co-occupancy analysis demonstrated that PATZ1 frequently co-bound with other stripe factors such as KLF7, SP1, SP2, and ZNF148/ZNF281, consistent with its proposed role as a stripe factor facilitating co-accessibility (Figure 5C, right panel, Table 5). The co-occurrence heatmap shows high cosine similarity (orange) between PATZ1 and these factors, indicating coordinated binding at shared regulatory elements. This widespread binding pattern and co-occupancy with multiple transcription factors suggests that PATZ1 functions as a developmental regulator of chromatin accessibility at growth-associated genes, potentially explaining its enrichment in injury-responsive regions where chromatin remodeling is required. Network analysis of PATZ1-bound genes in embryonic and postnatal neurons further confirmed enrichment for growth-relevant functions including regulation of cell growth, cytoskeleton organization, chromatin remodeling, DNA damage repair, and nervous system development, reinforcing PATZ1's potential role in coordinating the accessibility of pro-regenerative gene networks.

In summary, our data suggests that PATZ1 functions as a developmental regulator that enables chromatin accessibility at growth-associated genes during early neurodevelopment when regenerative capacity is high. The observed pattern of PATZ1 binding—high in young neurons, reduced in adults, and increased again after intracortical injury—points to its potential role as a key mediator of chromatin remodeling along growth regions in CNS neurons.

**PATZ1 Overexpression significantly enhances Chromatin Accessibility in Corticospinal tract neurons Following Spinal Cord Injury**

Based on the evidence that PATZ1 functions as a developmental regulator of chromatin accessibility, we sought to test whether PATZ1 overexpression could enhance accessibility following spinal cord injury. To investigate this question, we developed an experimental approach using AAV-mediated PATZ1 expression combined with thoracic crush injury (Figure 6A). Adult mice received intracranial injections of AAV-GFP (control) and AAV-PATZ1, followed by thoracic crush injury. After injury, motor cortices were dissected, nuclei isolated and FACS-sorted, and subjected to single-nucleus ATAC-seq (snATAC-seq) to assess changes in chromatin accessibility.

Dimensional reduction analysis of the snATAC-seq data revealed subtle but distinct chromatin accessibility profiles between injured control neurons and PATZ1-overexpressing injured neurons (Figure 6B). UMAP visualization showed separation between these populations, particularly along targeted regulatory regions rather than genome-wide changes. The bottom panels displaying feature plots for CST neuron marker genes (*Satb2, Lrp8, Etv1, Tnnc1, Crym,* and *Mrpl11*) confirm that both populations represent the same neuronal subtype, ensuring proper comparison. Quantification of accessibility changes revealed a substantial effect of PATZ1 overexpression, with 9,843 regions showing increased accessibility compared to only 5,482 accessible regions in control injured neurons - representing a 1.8-fold increase in the total number of accessible sites (Figure 6C, left panel, Table 6). Genomic distribution analysis showed that the majority (78%) of newly accessible regions were located at potential enhancers, with 22% at promoters (Figure 6C, right panel). PATZ1 overexpression increased the magnitude of accessibility changes, with a substantial portion of peaks showing log2FC values between 3.0-7.0 (approximately 8 to 128-fold increases in accessibility) compared to injured controls where the majority of peaks exhibited log2FC values below 2.5 (less than 5.7-fold changes). This difference in accessibility magnitude is clearly visible in the fold-change distribution histogram, where PATZ1 overexpression induced approximately 7,000 peaks with log2FC values greater than 3.0, compared to nearly none in the injured-only condition.(Table 6)

Gene Ontology (GO) analysis of the differentially accessible regions revealed stronger enrichment for critical regeneration-associated pathways in PATZ1-overexpressing neurons compared to injured controls (Figure 6D, Table 6). Chromatin remodelling (GO:0006338) was the most significantly enriched term in PATZ1-overexpressing neurons ($p<10^{-40}$), while showing only modest enrichment in injured controls. Other pathways showing substantially stronger enrichment in PATZ1-overexpressing neurons included nervous system development (GO:0007399), signal transduction (GO:0007165), cell differentiation (GO:0030154), and positive regulation of gene expression (GO:0010628). The size of the circles represents gene count, demonstrating that PATZ1 overexpression affected larger gene sets across nearly all functional categories. Notably, axon guidance (GO:0007411) was present in PATZ1-overexpressing neurons but absent in injured controls, suggesting a specific enhancement of regenerative pathways.

Detailed analysis of the distribution and magnitude of accessibility changes across key functional pathways revealed a shift in the strength of chromatin accessibility in PATZ1-overexpressing neurons (Figure 6E, Table 6). The circular plots illustrate the distribution of fold-change values (log2FC) across different ranges for each pathway, with PATZ1-overexpressing neurons (blue outlines) showing a substantial shift toward higher magnitude changes (2-4 log2FC and 3-4 log2FC ranges) compared to injured controls (red outlines) where most changes were concentrated in the lower magnitude ranges (0.5-1 log2FC and 1-2 log2FC). This shift toward higher magnitude changes was consistent across all examined pathways, including axon guidance, chromatin remodelling,

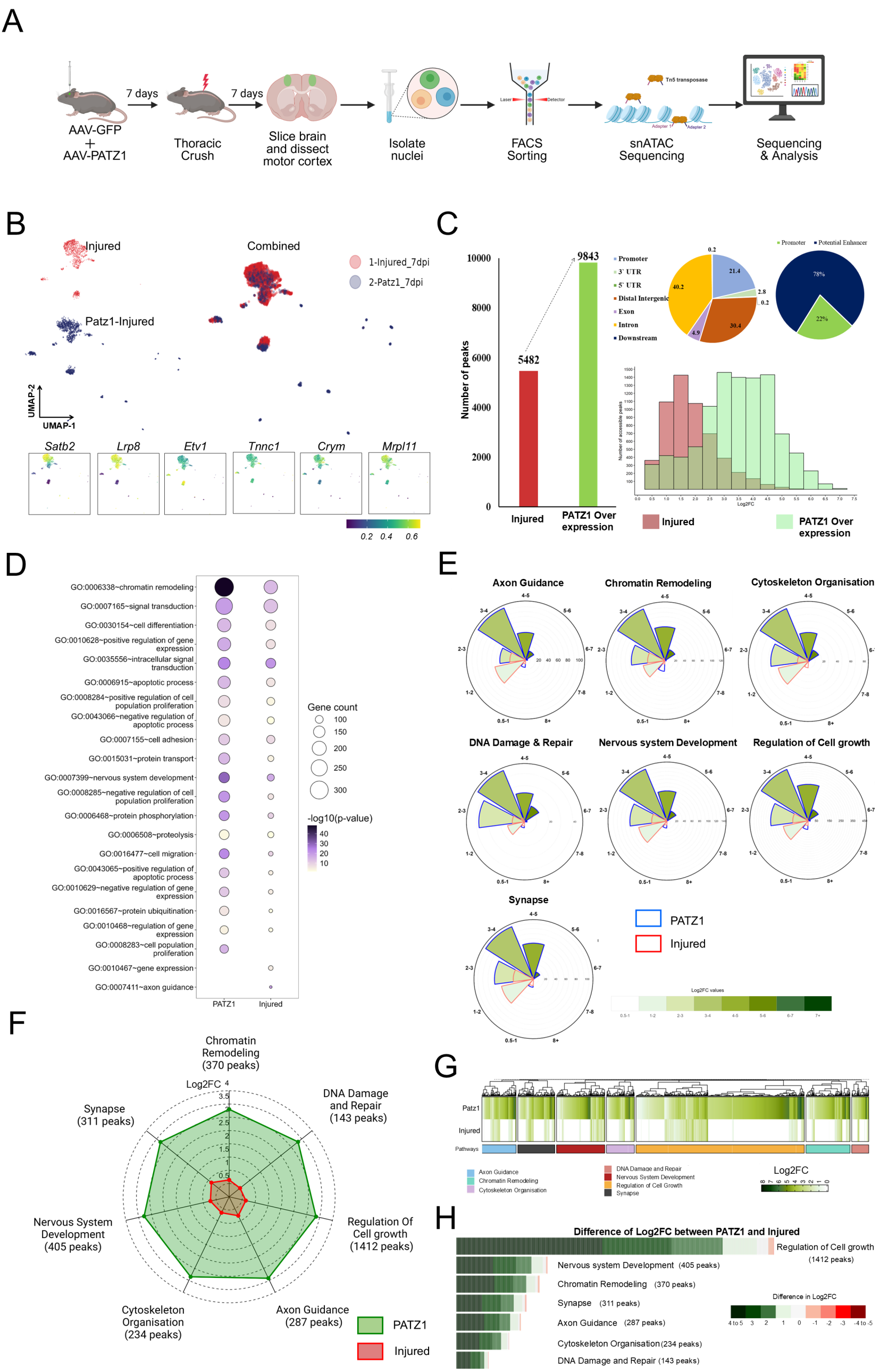


**Figure. 6 Single-nuclear (sn)ATAC-seq reveals that chromatin around pro-growth genes becomes more accessible upon PATZ1 over-expression**. (A) Schematic representation of single-nucleus ATAC-seq (snATAC) experimental workflow with AAV-PATZ1. (B) UMAP representation showing distinct clustering patterns between Injured control and PATZ1_Injured conditions. (C) Quantitative analysis demonstrating increased accessible chromatin regions in PATZ1 overexpression (9843) versus Injured control (5482). Pie charts displaying the genomic distribution of the PATZ1 over-expressed peaks. Histogram showing the number of accessible peaks in injured control (red) and upon PATZ1 over-expression (green). (D) Dot plot showing Top 20 Gene Ontology (GO) terms in PATZ1-overexpression versus injured control conditions. The size of dots represents the number of genes associated with each GO term, while colour intensity indicates statistical significance (-log10 p-value). (E) Circular plots comparing chromatin accessibility patterns between PATZ1-overexpressing (Blue bar) and control injured (orange bar) neurons across seven key biological pathways. Each plot displays the distribution of differential accessibility based on Log2 fold change (radial axis from 0 to 8) magnitude signified by the intensity of green shading. (F) Radar chart comparing the magnitude and distribution of chromatin accessibility changes between PATZ1-overexpressing (green) and control injured (red) neurons across seven key biological pathways. Each axis represents a distinct pathway with the total number of associated accessible peaks indicated in parentheses.The concentric circles represent Log2FC values ranging from 0.5 to 4.0. (G) Heatmap of differential accessibility across neuronal pathways, with colour intensity representing fold change. Colour intensity (green) represents fold change in accessibility, with annotated functional pathways.(p-value <0.05, Bonferroni correction, FDR <0.05). (H) Horizontal bar graph displaying the difference in Log2FC values of chromatin accessibility between PATZ1-overexpressing and injured control neurons across seven key biological pathways.The colour scale ranges from dark green (strong positive difference, indicating greater accessibility in PATZ1-overexpressing neurons) to red (negative difference, indicating reduced accessibility).

cytoskeleton organization, DNA damage and repair, nervous system development, regulation of cell growth, and synaptic function.

The radar plot in Figure 6F (Table 6) provides a comprehensive quantification of the differences in chromatin accessibility between PATZ1-overexpressing and control injured neurons across key functional pathways. PATZ1 overexpression expanded both the number and magnitude of accessible regions, with average log2FC values of approximately 3.0 across all pathways compared to just 0.5-1.0 in injured controls. The most pronounced effects were observed in regulation of cell growth (1412 peaks in PATZ1 vs. minimal peaks in injured controls), nervous system development (405 peaks), chromatin remodelling (370 peaks), synaptic function (311 peaks), axon guidance (287 peaks), cytoskeleton organization (234 peaks), and DNA damage repair (143 peaks). This visualization shows how PATZ1 overexpression transforms the injury response, creating a more robust chromatin accessibility profile.

Hierarchical clustering analysis of differentially accessible regions confirmed the distinct regulatory patterns between PATZ1-overexpressing and control injured neurons (Figure 6G, Table 6). The heatmap reveals consistent increases in accessibility (brighter green) across all pathways in PATZ1-overexpressing neurons compared to the more limited pattern in injured controls. The bottom annotation bars identify the specific pathways, with regulation of cell growth (orange) representing the largest category. Quantification of the difference in accessibility (Figure 6H, Table 6) demonstrates that PATZ1 overexpression had the strongest impact on regulation of cell growth and nervous system development (with many peaks showing 4-5 log2FC difference), followed by chromatin remodelling, synaptic function, axon guidance, cytoskeleton organization, and DNA damage repair. These differences were overwhelmingly positive (green bars), indicating that PATZ1 consistently enhanced rather than diminished accessibility. Together, these findings demonstrate that PATZ1 overexpression enhances injury-induced chromatin remodelling by 6-8 fold, targeting key pathways associated with axon growth and regeneration.

**PATZ1 Activates Developmental Gene Programs in Adult CNS Neurons After Injury**

To determine whether the extensive chromatin accessibility changes induced by PATZ1 overexpression translate to functional transcriptional activation, we performed combined single-nucleus RNA-seq and ATAC-seq analysis following spinal cord injury (Figure 7A). Using the same experimental paradigm, we administered AAV-GFP (control) and AAV-PATZ1 to adult mice, performed thoracic crush injury, and then isolated nuclei from motor cortices for parallel snRNA-seq and snATAC-seq analysis. Dimensional reduction analysis of the snRNA-seq data revealed distinct transcriptional profiles across multiple cell clusters (Figure 7B, left). The feature plots for established CST neuron markers (*Satb2, Ccnd2, Etv1, and Crym*) confirmed successful isolation of layer 5 projection neurons (Figure 7B, right), ensuring that our analysis focused specifically on the injury-responsive neuronal population. Differential gene expression analysis between PATZ1-overexpressing and control injured neurons revealed substantial transcriptional changes, with 1,825 genes upregulated

and 4,369 genes downregulated across different fold-change thresholds (Figure 7C, Table 7). Notably, we observed a gradient in the magnitude of differential expression, with 1,383 genes upregulated and 2,466 genes downregulated in the 0.5-1 log2FC range, while 27 genes were upregulated and 141 genes downregulated by more than 4-fold (log2FC ≥ 4).

To further characterize the relationship between PATZ1-induced chromatin accessibility changes and transcriptional activation, we performed an integrative analysis of snATAC-seq and snRNA-seq data (Figure 7D-F, Table 7). The Venn diagram (Figure 7D) illustrates the overlap between accessible chromatin regions and differentially expressed genes in PATZ1-overexpressing neurons compared to injured controls. We identified 4,483 regions that were accessible but not associated with differential gene expression (blue), 523 regions that were both accessible and transcriptionally active (green), and 1,131 genes that were differentially expressed despite no detectable changes in chromatin accessibility (gray). Gene Ontology analysis of these distinct categories revealed pathway-specific patterns. Regions that were accessible but not transcribed were enriched for chromatin remodeling (GO:0006338), positive regulation of DNA-templated transcription (GO:0045893), and signal transduction (GO:0007165), suggesting that PATZ1 establishes a permissive chromatin state that may require additional factors for transcriptional activation. Regions that were both accessible and transcribed showed strong enrichment for nervous system development (GO:0007399), chromatin remodeling (GO:0006338), and axon guidance (GO:0007411), indicating that a subset of the PATZ1-opened chromatin regions successfully recruited the necessary transcriptional machinery to activate regeneration-associated genes. Intersection analysis of gene ontology (GO) terms between accessible regions (ATAC peaks), transcribed genes (RNA), and genes that are both accessible and transcribed (Figure 7E, Table 7) revealed 124 GO terms uniquely enriched in the accessible and transcribed gene set. Further analysis of highly accessible and highly transcribed genes revealed enrichment for functional categories including cell cycle regulation, DNA repair and maintenance, cell structure and organization, redox and oxidative stress, Signalling pathways, metabolism, development, and stem cell fate determination (Table 7). We also identified a significant set of genes that were downregulated in PATZ1-overexpressing neurons (Figure 7F, Table 7), with 4,199 peaks accessible but not associated with transcriptional changes, 807 accessible regions associated with decreased expression, and 2,504 genes with decreased expression without accessibility changes. GO analysis and semantic space clustering of these downregulated genes revealed enrichment for pathways related to homeostasis, signalling, stem cell fate, transport, and immune response, suggesting that PATZ1 overexpression may selectively suppress these functions while promoting growth and regeneration pathways.

In summary, our integrated epigenomic and transcriptomic analysis demonstrates that PATZ1 overexpression drives a coordinated program of chromatin remodeling and gene expression changes that may favour developmental growth-associated pathways in CNS neurons following spinal cord injury. The activation of these pathways, which are typically active during early developmental stages

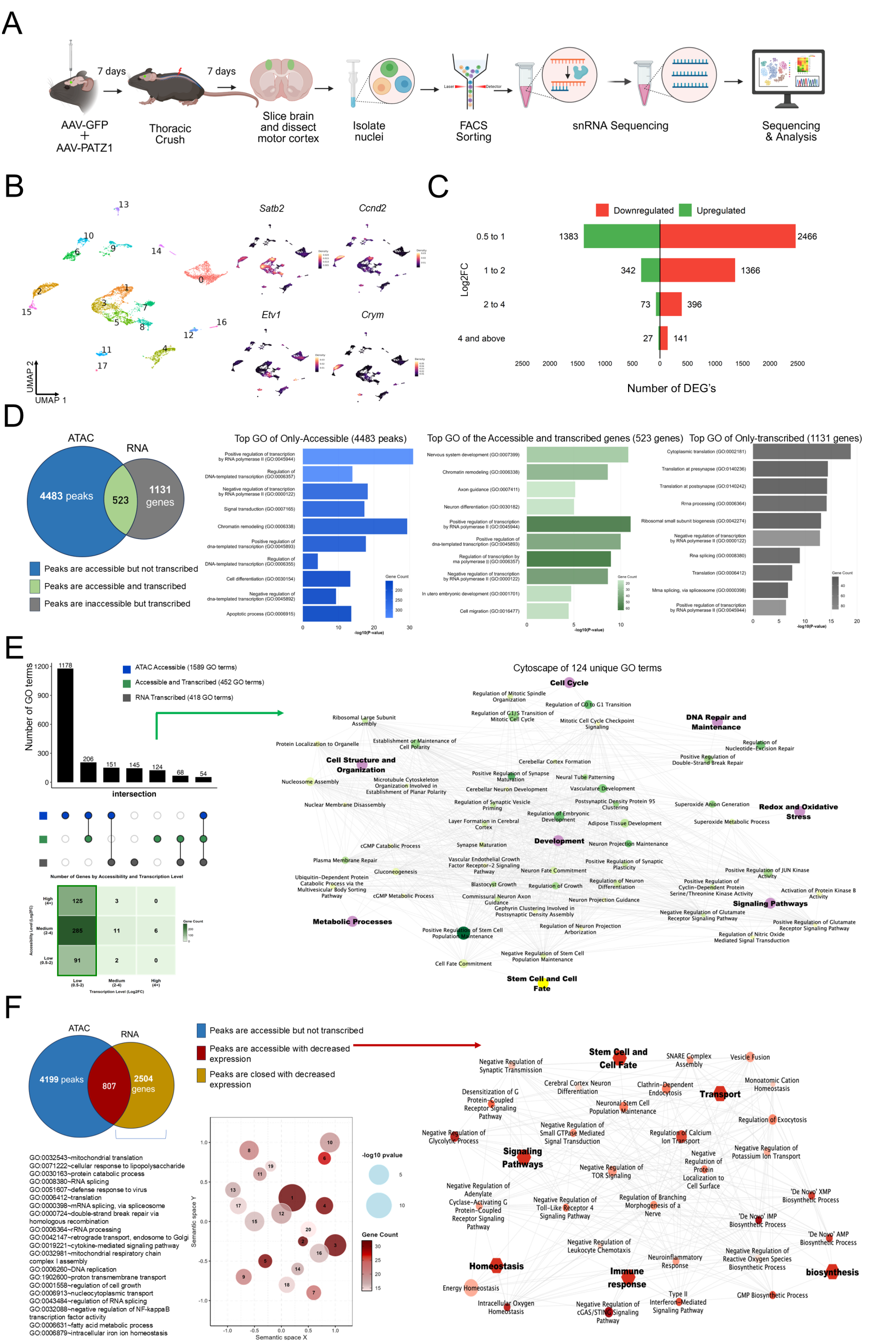


**Figure 7. Integrative analysis of single-nucleus RNA sequencing and ATAC sequencing reveals transcriptional and chromatin accessibility profiles in PATZ1 tissue sample**. (A) Schematic illustration of the experimental workflow. (B)UMAP visualisation of single-nucleus RNA-seq (snRNA-seq) data from the PATZ1 sample. (C) Distribution of differentially expressed genes (DEGs) by fold change categories. The horizontal bar plot displays the number of upregulated (green) and downregulated (red) genes across four log2 fold-change ranges (0.5 to 1, 1 to 2, 2 to 4, and 4 and above)indicating the exact count of DEGs within each category. (D)Left: Venn diagram showing the overlap between accessible chromatin peaks identified by ATAC-seq (4483 peaks) and transcribed genes identified by RNA-seq (1131 genes), with 523 features showing both accessibility and transcription. Right: Gene Ontology (GO) enrichment analysis for: (i) only-accessible peaks, (ii) accessible and transcribed genes, and (iii) only-transcribed genes.($p<0.05$). (E) Comprehensive analysis of accessible and transcribed Gene Ontology (GO) terms. Top: Upset plot comparing the number of ATAC-accessible GO terms (1589), accessible and transcribed GO terms (432), and RNA transcribed GO terms (418). Right: Gene Ontology (GO) enrichment analysis of unique terms enriched by accessible and transcribed genes.Bottom: Heatmap showing gene distribution across transcription levels and accessibility categories. (F) Left: Venn diagram identifying peaks accessible but not transcribed (blue), accessible with increased expression (red, 807 peaks), and closed with decreased expression (yellow, 2504 genes). Middle: Bubble plot of enriched GO terms of downregulated genes with inaccessible peaks, with point size indicating significance and color representing gene count($p<0.05$).Right: Gene Ontology (GO) enrichment analysis of terms enriched by accessible and downregulated 807 genes.

when axon growth capacity is high, may potentially contribute to enhanced regenerative capacity after CNS injury.

**Histone Acetylation and CTCF Binding Dynamics After Spinal Cord Injury reveals targeted response to thoracic injury**

Since our analyses revealed significant enhancer-mediated regulation in CNS neurons, we sought to investigate the dynamics of H3K27ac (a marker of active enhancers) and CTCF (which defines chromatin domain boundaries) following thoracic spinal cord injury. We employed Cleavage Under Targets and Release Using Nuclease (CUT&RUN), a technique that provides high-resolution mapping of protein-DNA interactions with lower background than traditional ChIP-seq (Figure 8A). This approach involves antibody targeting of specific chromatin proteins in permeabilized nuclei, followed by protein A-MNase binding, calcium-activated cleavage of antibody-bound regions, and sequencing of the released DNA fragments.

H3K27ac profiling revealed both common and unique acetylation patterns between uninjured and injured conditions (Figure 8B). We identified 483 regions with H3K27ac exclusively in uninjured neurons, 690 regions common to both conditions, and 444 regions uniquely acetylated after injury. Genomic browser tracks of representative loci (*Fosb, Cdh11, Sorcs3, Dmrt2, Klf3a,* and *Tuft1*) illustrate these differential patterns (Table 8). Gene Ontology analysis of differentially acetylated regions (Figure 8C-D, Table 8) revealed that common pathways between conditions included transcriptional regulation, nervous system development, chromatin remodeling, and axon guidance. Regions gaining H3K27ac after injury were enriched for cell adhesion, intracellular signal transduction, synaptic transmission, extracellular matrix organization, and neurogenesis (Figure 8D), suggesting activation of plasticity-related processes that may facilitate adaptive responses to injury. In contrast, regions losing H3K27ac were associated with transcriptional regulation, cytoskeleton organization, and cilium assembly, potentially indicating downregulation of normal maintenance functions to prioritize injury response. Notably, most differential H3K27ac sites were concentrated within 0-10kb of transcription start sites (Figure 8E), with gained sites showing a broader distribution extending up to 20kb from promoters, suggesting that injury induces both proximal and distal regulatory changes.

CTCF binding analysis revealed extensive reorganization of chromatin boundaries after injury, with 725 sites losing CTCF binding and 1,421 sites gaining CTCF binding (Figure 8F-H, Table 8). Regions gaining CTCF binding were significantly enriched for negative regulation of DNA-templated transcription, regulation of DNA-templated transcription, and intracellular signal transduction (Figure 8G), suggesting establishment of new regulatory domains that may control injury-specific gene expression programs. Regions losing CTCF were associated with negative regulation of apoptotic processes, cell migration, and positive regulation of gene expression, potentially reflecting disruption

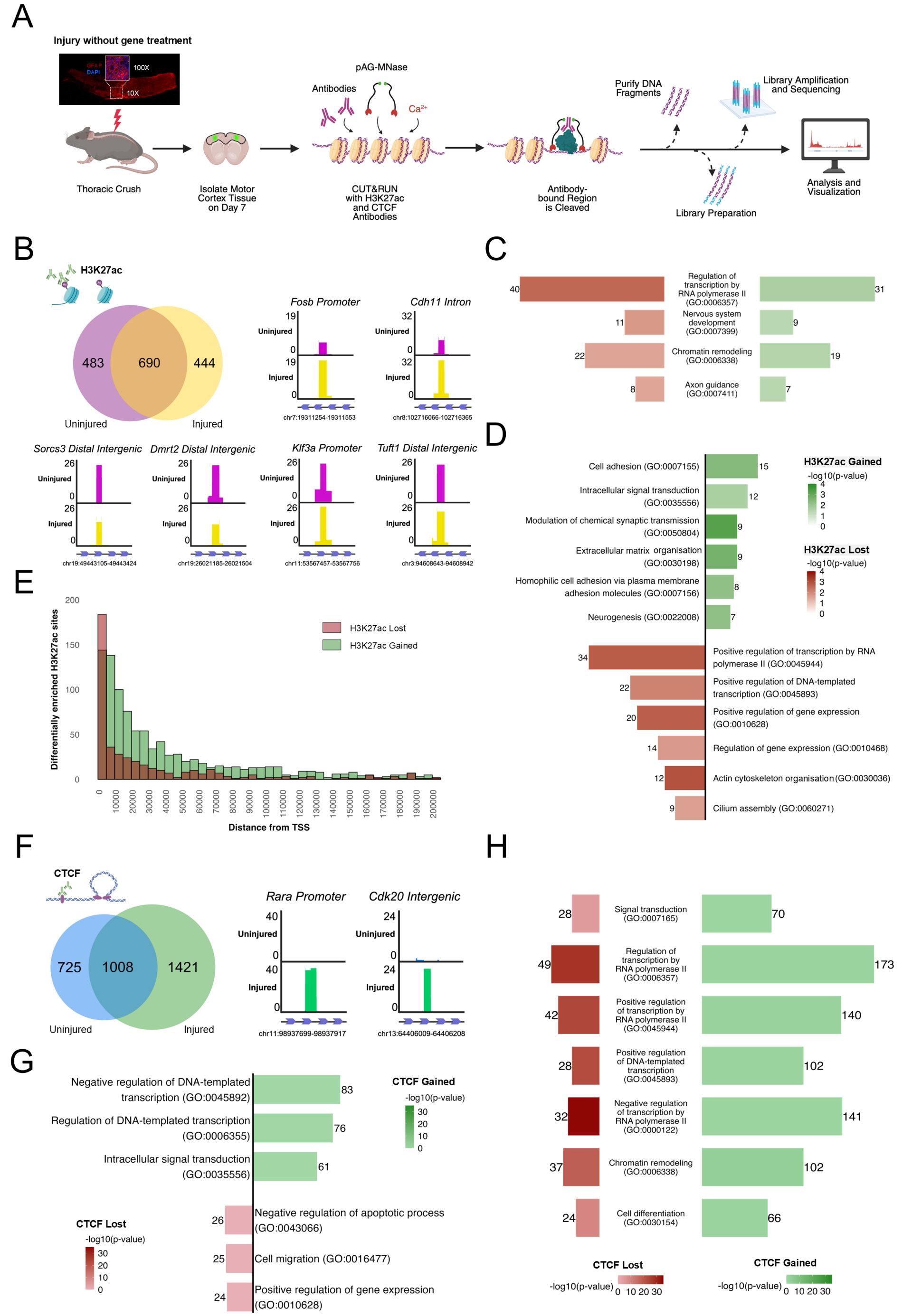


**Figure 8. Genome-wide profiling of H3K27ac and CTCF binding using CUT&RUN.**(A) Schematic overview of the CUT&RUN experimental strategy. (B)Venn diagram comparing H3K27ac regions between uninjured (purple) and injured (yellow) conditions, showing 483 unique, 690 overlapping, and 444 unique regions, along with a representative genomic locus displayed using the UCSC genome browser. (C) Gene Ontology (GO) pathways commonly enriched in H3K27ac-marked regions following injury, showing H3K27ac lost (red) and H3K27ac gained (green) categories. (D) GO pathways uniquely enriched in H327ac regions in the injured, where unique H3k27ac is lost upon injury (red), and unique H3K27ac terms are gained upon Injury (green). (E) Genomic distribution of distance of H3K27ac peaks relative to transcription start sites (TSS) between H3k27ac gained(green) and lost (red). (F) Venn diagram comparing CTCF regions between uninjured (blue) and injured (green) conditions, showing 725 unique, 1008 overlapping, and 1421 unique regions with representative genome browser tracks. (G) GO pathways uniquely enriched in CTCF binding sites upon injury. Left side shows pathways for CTCF Lost (red bars) Right side shows pathways for CTCF Gained (green bars). (H) GO pathways commonly enriched in CTCF binding sites across both conditions. Horizontal bar chart of GO pathways commonly enriched in CTCF binding sites, with red bars (CTCF Lost ) and green bars (CTCF Gained)

of homeostatic chromatin organization to permit specialized injury responses. Pathway analysis of common CTCF-bound regions showed substantially more binding sites in the injured condition across all key pathways (Figure 8H), including signal transduction (70 vs. 28), regulation of transcription (173 vs. 49), positive regulation of transcription (140 vs. 42), positive regulation of DNA-templated transcription (102 vs. 28), negative regulation of transcription (141 vs. 32), chromatin remodeling (102 vs. 37), and cell differentiation (66 vs. 24). This increased CTCF binding after injury suggests formation of new chromatin loops and territories that may facilitate coordinated regulation of injury-response genes while maintaining proper insulation from non-relevant genomic regions.

In summary, our CUT&RUN analysis reveals that spinal cord injury induces significant remodeling of the epigenetic landscape in CST neurons, characterized by targeted H3K27ac modifications at growth and synaptic pathways and extensive reorganization of CTCF-mediated chromatin architecture. These changes suggest that injury triggers a coordinated program of enhancer activation and boundary reorganization that may contribute to the limited but targeted epigenetic response observed after thoracic injury.

**PATZ1 overexpression in injured CST neurons induces Widespread H3K27ac Deposition and CTCF Boundary Reorganization**

Having established that PATZ1 overexpression enhanced chromatin accessibility and gene expression, we next sought to characterize the direct binding patterns of PATZ1 and their effect on histone acetylation and chromatin boundaries in the injured CNS. We employed CUT&RUN to map PATZ1 binding sites in mice that received AAV-PATZ1 prior to thoracic spinal cord injury (Figure 9A). Genomic distribution analysis of 5,803 PATZ1 binding sites revealed that the vast majority (86.2%) were located at potential enhancers, with only 13.8% at promoters (Figure 9B, Table 9). Browser tracks of representative loci demonstrated that PATZ1 bound to key regulatory elements of growth-associated genes, including intergenic regions near *Klf7* and *Lgals1*, an intronic region within *Stat3*, and the *Sox11* promoter (Figure 9C). Further examination of PATZ1 binding at different types of regulatory elements showed clear enrichment at promoters (*Sgol1*) and both proximal and distal enhancers (*Rarg* and *Rara*) (Figure 9D). Classification of PATZ1-bound regions by regulatory element type revealed that 36.60% mapped to distal enhancer-like elements, 23.03% to CTCF-only sites, 22.55% to proximal enhancer-like elements, 13.89% to promoter-like sites, and 3.83% to DNase-H3K4me3 sites (Figure 9E, left, Table 9). Interestingly, CTCF motifs were enriched near PATZ1 binding sites, with the highest frequency observed in regions far (>100kb) from PATZ1 binding (Figure 9E, right).

To determine how PATZ1 binding affects histone acetylation patterns, we compared H3K27ac profiles between injury-only and PATZ1-treated injured samples. PATZ1 treatment dramatically expanded H3K27ac-marked regions, with 2,847 regions uniquely acetylated in PATZ1-treated neurons compared to injury-only samples, representing an 11.6-fold increase over the 246 unique regions in the injury-

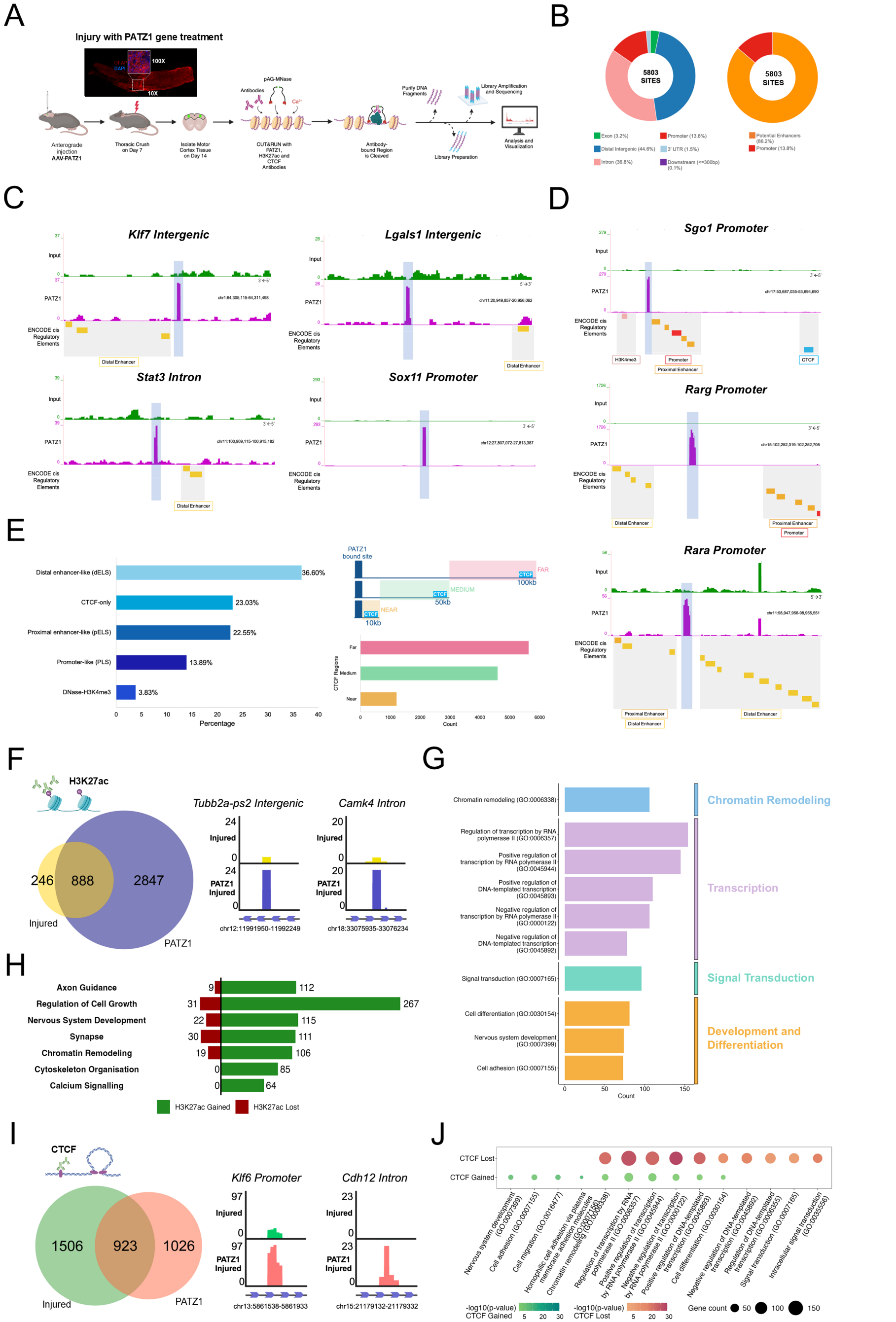


**Figure 9. Genome-wide profiling of PATZ1 binding sites using CUT&RUN.** (A) Schematic of the CUT&RUN workflow for mapping PATZ1 binding sites. (B) Genomic distribution of 5803 PATZ1-bound regions (left) and regulatory element classification: Potential Enhancers (86.2%) and Promoters (13.8%) (right). (C) Genome browser tracks showing PATZ1 binding (pink) at intergenic regions of pro-growth genes (*Klf7*, *Lgals1*, *Stat3* Intron, and *Sox11* Promoter). Yellow bars: ENCODE regulatory elements; blue-shaded areas: distal enhancers. (D) PATZ1 binding patterns at cis-regulatory elements showing Input (green), PATZ1 binding (pink/purple), and ENCODE elements (yellow) at *Spg1* and *Rarb* Promoter regions. (E) Distribution of PATZ1 binding at cis-regulatory elements (left): distal enhancer-like (36.60%), CTCF-only (23.03%), proximal enhancer-like (22.55%), promoter-like (13.89%), and DNase-H3K4me3 (3.83%). Right: CTCF motif enrichment relative to PATZ1 binding sites by distance. (F) Overlap of H3K27ac-enriched regions between injured (246 unique) and PATZ1-treated injured samples (2847 unique), with 888 shared regions. Right: Browser views showing PATZ1-dependent H3K27ac enrichment (blue) compared to injured-only samples (yellow). (G) GO analysis of H3K27ac regions unique to PATZ1-treated injured samples. (H) Regeneration-associated pathways enriched in H3K27ac-marked regions: gained (green) and lost (red) in PATZ1-treated injured samples. (I) Overlap of CTCF binding sites between injured (1506 unique) and PATZ1-treated injured (1026 unique) samples, with 923 shared sites. Right: Browser tracks showing condition-specific CTCF peaks. (J) GO analysis showing pathways with CTCF lost (pink) and gained (green) between conditions. Dot size: gene count; color intensity: significance (-log10(p-value).

only condition (Figure 9F, left, Table 9). Browser tracks of representative loci (*Tubb2a-ps2* and *Camk4*) confirmed the substantial increase in H3K27ac deposition following PATZ1 treatment (Figure 9F, right). Gene Ontology analysis of H3K27ac regions unique to PATZ1-treated samples revealed enrichment for pathways related to transcription (regulation and positive regulation of RNA polymerase II-mediated transcription), chromatin remodeling, signal transduction, and development/differentiation (Figure 9G, Table 9). This enrichment pattern suggests that PATZ1 treatment selectively enhances the activation of gene programs involved in growth and plasticity while simultaneously promoting chromatin reorganization required for transcriptional activation. Quantification of H3K27ac changes at specific regeneration-associated pathways showed substantial gains in acetylation, with minimal losses across axon guidance (112 gained vs. 9 lost), regulation of cell growth (267 vs. 31), nervous system development (115 vs. 22), synaptic function (111 vs. 30), chromatin remodeling (106 vs. 19), cytoskeleton organization (85 vs. 0), and calcium Signalling (64 vs. 0) (Figure 9H, Table 9).

PATZ1 treatment also induced significant reorganization of CTCF-mediated chromatin boundaries. Comparison of CTCF binding sites between injury-only and PATZ1-treated conditions revealed 1,506 sites unique to injury, 1,026 sites unique to PATZ1 treatment, and 923 shared sites (Figure 9I, left). Browser tracks of representative loci (*Klf6* and *Cdh12*) illustrated this differential binding, with CTCF occupying the *Klf6* promoter significantly more in PATZ1-treated samples and the *Cdh12* intron exclusively in PATZ1-treated samples (Figure 9I, right, Table 9). Gene Ontology analysis of differential CTCF binding demonstrated distinct functional enrichment patterns between conditions (Figure 9J, Table 9). Notably, pathways related to nervous system development, cell adhesion, cell differentiation, cell migration, and extracellular matrix organization showed greater CTCF gain in PATZ1-treated samples, while a loss in CTCF was observed in genes related to transcription, differentiation and signal transduction. This pattern suggests that PATZ1 may be altering three-dimensional chromatin architecture by removing insulator boundaries that normally restrict enhancer-promoter interactions in these growth-associated pathways. By reducing CTCF binding at these specific loci, PATZ1 may be enabling long-range interactions between enhancers and promoters that would otherwise be blocked by CTCF-mediated domain boundaries. This selective reorganization of chromatin domains could enhance the transcriptional activation of regeneration-associated genes by facilitating their interaction with distal regulatory elements, potentially recapitulating a permissive chromatin state similar to that observed in developing or regeneration-competent neurons.

In summary, our CUT&RUN analysis reveals that PATZ1 predominantly binds to enhancer regions of growth-associated genes and induces widespread H3K27ac deposition while reorganizing CTCF-mediated chromatin boundaries. These findings suggest that PATZ1 functions as a master regulator of chromatin state in CNS neurons, coordinating both enhancer activation and three-dimensional chromatin architecture to facilitate targeted gene expression programs supportive of axon growth.

**PATZ1 orchestrates targeted 3-D chromatin reorganization around growth-relevant loci**

To elucidate the mechanisms underlying PATZ1-mediated enhancement of regenerative capacity, we employed Hi-C (High-throughput Chromosome Conformation Capture) to analyze three-dimensional chromatin architecture in motor cortex tissue following thoracic crush injury (Fig. 10A). Hi-C technology captures genome-wide chromatin interactions, allowing identification of compartments (A/B, representing active/inactive chromatin regions) and topologically associating domains (TADs, self-interacting chromatin regions that regulate gene expression).

Contact matrices at 5Mb and 50kb resolution revealed specific alterations in chromatin organization following PATZ1 expression (Fig. 10B). Principal component analysis demonstrated that PATZ1 induces targeted rather than broad chromatin reorganization, with only 3.5% of genomic regions transitioning from B to A compartments and 2.9% shifting from A to B compartments (Fig. 10C, Table 10). These limited yet specific changes suggest PATZ1 acts through precise modulation of chromatin architecture rather than global reorganization.

Gene ontology analysis of these compartment-switching regions revealed striking functional dichotomy. Regions transitioning from inactive (B) to active (A) compartments were significantly enriched for genes involved in energy homeostasis, cell adhesion, signal transduction, and nervous system development (Fig. 10D, left, Table 10). This suggests PATZ1 selectively activates chromatin regions containing genes essential for cellular energetics, intercellular communication, and neural regeneration pathways. Particularly notable was the enrichment of chromatin remodeling genes, indicating potential feed-forward mechanisms that could amplify PATZ1's effects on chromatin architecture.

Conversely, regions shifting from active (A) to inactive (B) compartments were enriched for genes involved in negative regulation of transcription, cell population proliferation, and apoptotic processes (Fig. 10D, right, Table 10). This compartment repression pattern suggests PATZ1 strategically silences chromatin regions containing genes that would otherwise limit regenerative capacity through growth inhibition or programmed cell death. Intriguingly, both A→B and B→A transitions showed enrichment for chromatin remodeling genes, suggesting PATZ1 may orchestrate a comprehensive reorganization of chromatin regulatory networks.

Detailed analysis of the 799 regions that shifted to A compartment showed that while 36.8% became differentially accessible, only 3.1% exhibited differential transcription (Fig. 10E, Table 10). This discrepancy indicates that compartment shifts predominantly establish a permissive chromatin environment that may prime genes for activation upon subsequent stimuli, rather than directly driving transcriptional changes.

TAD analysis revealed substantial restructuring of chromatin domains, with 2500 PATZ1-unique TADs (domains present only in PATZ1-treated samples) and 2602 shifted TADs (domains present in both conditions but with altered boundaries) compared to injury controls (Fig. 10G). Shifted TADs represent

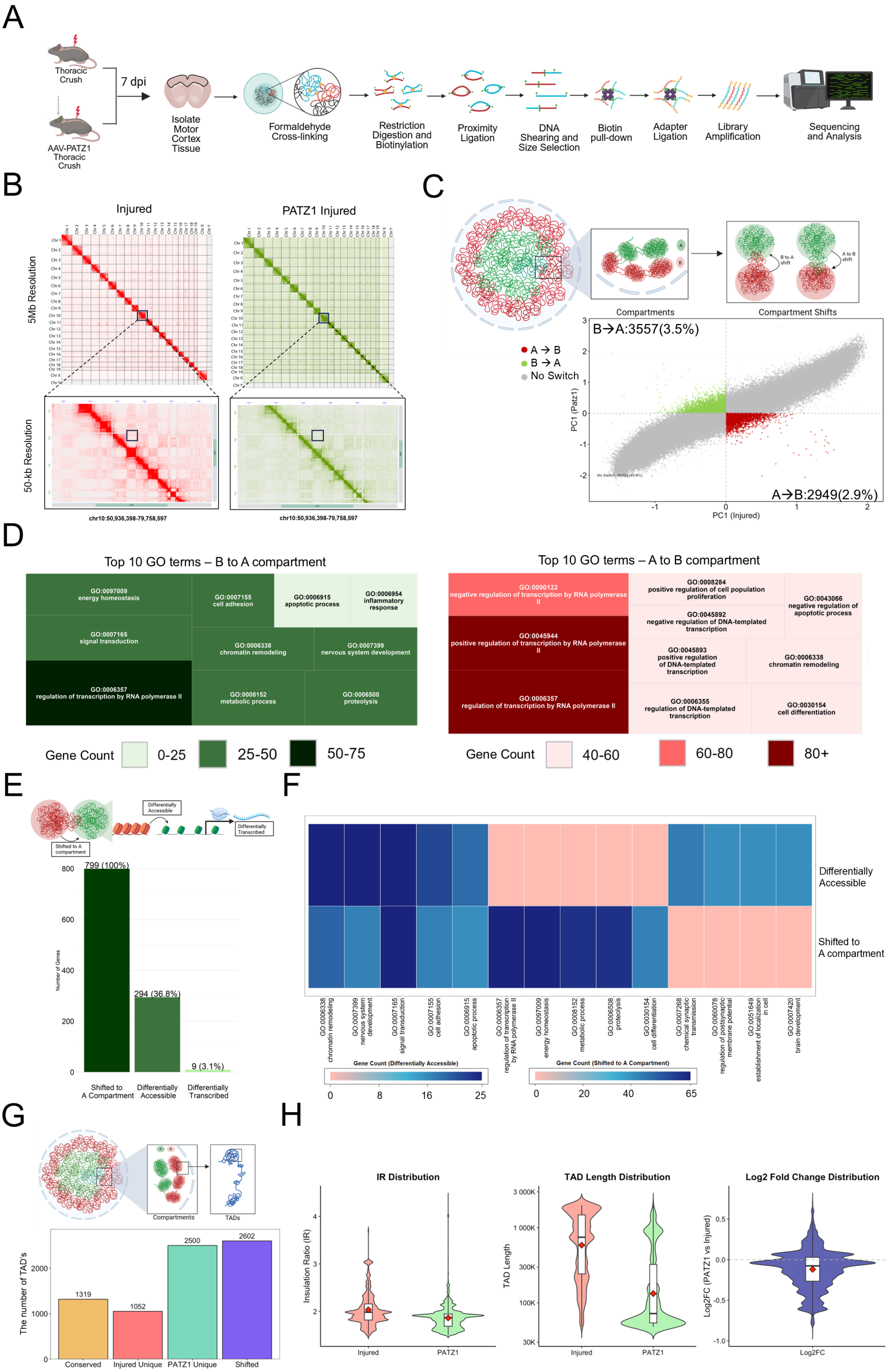


**Figure 10. Functional analysis of compartment switching by PATZ1.** (A) Experimental workflow for Hi-C analysis. (B) Contact matrices displaying chromatin interactions at 5Mb (left) and 50kb (right) resolution. Upper red matrices and lower green matrices represent two control(Injured) and Patz1 injured samples, with signal intensity values indicated. (C)Top: Depicts a model of nuclear organisation showing A/B compartmentalisation (green/red) and compartment shifts between conditions. Bottom: The bottom scatterplot shows principal component analysis of genomic regions, with points colored by compartment switching status: B→A regions (3557 regions, 3.5% of total) in green, A→B regions (2949 regions, 2.9%) in red, and non-switching regions in gray. The x-axis shows principal component (PC) values of the injured condition, while the y-axis shows principal component (PC) values of the PATZ1 condition. (D) Hierarchical representation of the top 10 Gene Ontology(GO) terms enriched in B→A compartment switches (left, green) and A→B compartment switches (right, red). Colour intensity indicates gene count.($p<0.05$). (E) Bar graph showing the number of genomic regions that shifted to A compartment (799, 100%), became differentially accessible (294, 36.8%), and were differentially transcribed (9, 3.1%). (F) Heatmap showing the relationship between differentially accessible regions (top row) and regions shifted to A compartment (bottom row) across various GO terms and biological processes. Colour intensity represents gene count. ($p<0.05$). (G).Quantification of Topologically Associating Domains (TADs) across categories showing conserved (1319), Injured-unique (1052), PATZ1-unique (2500) and shifted (2602). (H)Distribution comparisons between Injured (red) and PATZ1 (green) conditions: IR values (left), TAD lengths (middle), and Log2FC read counts (right).

regions where domain boundaries have relocated, potentially altering gene-enhancer interactions and regulatory insulation between neighboring genomic regions (Table 10). This extensive TAD reorganization suggests PATZ1 reconfigures the regulatory landscape through redefinition of chromatin domain boundaries.

PATZ1 expression resulted in dramatically smaller TADs (Fig. 10H, middle, Table 10), indicating more refined chromatin organization that could enable more precise control of gene regulatory interactions. Smaller TADs may facilitate more specific enhancer-promoter interactions by reducing the genomic distance between regulatory elements. Analysis of insulation ratios showed subtle differences between conditions, suggesting PATZ1 alters boundary strength at specific genomic loci. The symmetrical distribution of contact frequency changes with slight negative bias indicates selective reduction in certain long-range interactions following PATZ1 treatment (Fig. 10H, right, Table 10).
Collectively, these results demonstrate that PATZ1 enhances regenerative capacity through targeted chromatin reorganization that simultaneously activates regenerative pathways while suppressing inhibitory programs. The strategic compartment switching and TAD restructuring establish a permissive chromatin environment that may prime the genome for enhanced regenerative responses, providing a mechanistic basis for PATZ1's role in promoting tissue repair.

**Discussion**

Through a combination of epigenomic profiling, developmental time-course mapping, and targeted transcription-factor experiments, we show that PATZ1 can actively reshape chromatin structure in CNS neurons. We track how accessibility at growth-related loci narrows during maturation, then demonstrate that PATZ1 reopens these regions, driving compartment shifts and TAD reorganization that restore pro-growth gene programs. Our work pinpoints key epigenetic bottlenecks to axon regeneration and outlines a chromatin-focused approach to boost the intrinsic regenerative capacity of adult neurons.

Our developmental analysis revealed distinct temporal dynamics in chromatin restriction, with two discrete waves occurring during postnatal development rather than a continuous process. Growth-associated regulatory elements initially show gradual accessibility changes during early postnatal development (P0-P4), primarily involving partial restriction across many elements. This is followed by a more severe restriction phase between P7 and adulthood, coinciding with the completion of major developmental growth programs. Notably, we observed differences in the restriction patterns between promoters and enhancers, with some enhancer elements maintaining accessibility longer than their corresponding promoters, particularly those associated with nervous system development and DNA repair. Transcription factor footprinting identified distinct stage-specific binding landscapes, transitioning from growth-promoting factors in early development to maintenance-associated factors in adulthood. This temporal and pathway-specific restriction pattern provides crucial insights into the mechanisms underlying the developmental loss of regenerative capacity in CNS neurons.

Previous transcriptional studies have shown that injury proximity strongly influences the gene expression response of CNS neurons, with robust activation following intracortical injury and minimal changes after cervical or thoracic lesions(6). Our chromatin accessibility data extend these observations by revealing that distal injuries, such as thoracic spinal injury, also fail to elicit substantial epigenomic remodeling. While thoracic injuries induce modest chromatin changes at growth-associated loci, these are nearly ten-fold fewer than those observed after intracortical injury. This limited chromatin response likely contributes to the muted transcriptional activation seen in distal injuries and may result from the absence of key transcription factors or chromatin remodelers. Importantly, our findings parallel previous work that demonstrated that peripheral sensory neurons mount a robust chromatin opening response after sciatic nerve injury—a response that is largely absent in CNS neurons after spinal cord injury(38). Our data refine this dichotomy by showing that chromatin responsiveness in the CNS is not entirely lost but varies with injury context. Intracortical injury, unlike distal spinal injury, can still trigger widespread accessibility changes, suggesting that CNS neurons retain some latent epigenetic plasticity. Together, these results highlight injury proximity as a critical determinant of chromatin remodeling capacity and reinforce the idea that targeting chromatin regulators—particularly in the context of distal injuries—may help overcome intrinsic regenerative barriers in the adult CNS.

PATZ1 is a POZ/BTB and AT-hook domain-containing zinc finger protein with well-established roles in development, stem cell maintenance, and gene regulation (42–45). Its expression is high during early neurogenesis, concentrated in proliferating neural progenitors of the neocortical neuroepithelium, and tapers off toward adulthood—though it remains detectable in neurogenic niches (43). Genetic studies show that PATZ1 is essential for neural stem cell proliferation, with its loss leading to hypoplasia of periventricular regions (45). It also interacts with core pluripotency factors like Nanog and Pou5f1 to sustain embryonic stemness (42, 44). More recently, PATZ1 was identified as a member of the "stripe" transcription factor family, which binds GC-rich DNA to help maintain open chromatin, recruit additional transcription factors, and stabilize their binding at regulatory elements(41). This chromatin-opening role aligns with our findings of PATZ1 binding at growth-associated loci and its ability to reorganize chromatin in injured CNS neurons. Our data also connect PATZ1's function to a broader biological theme observed in regeneration-competent peripheral neurons, which transiently downregulate their subtype identity and activate a shared injury-response program—a shift thought to reflect temporary cellular plasticity. PATZ1's dual roles in maintaining developmental plasticity and driving chromatin remodeling suggest it may be a key enabler of this regenerative switch. Whether PATZ1 alone, or in synergy with other pro-regenerative factors, can translate epigenetic reprogramming into true functional regeneration remains to be tested—but it opens a compelling direction for CNS repair strategies rooted in chromatin biology.

Our finding that PATZ1 primarily binds to and activates enhancer regions underscores a growing consensus: enhancers are central to the gene regulatory programs that support axon regeneration. In earlier work, we showed that the pro-growth TF duo *Nr5a2*/KLF6 also acts predominantly at enhancers to promote axon regrowth *in vivo(22)*. This enhancer-centric regulation is echoed in peripheral neurons, where sciatic injury drives widespread chromatin opening at enhancers—far more than in central axotomy models—suggesting that enhancer activation is a hallmark of successful regenerative responses (38). Our current data go further, connecting this enhancer activity to the broader architecture of the genome. Hi-C analysis following PATZ1 overexpression revealed reorganization of 3D genome topology, including targeted TAD restructuring and compartment switching. These changes mirror recent reports from peripheral sensory neurons where regeneration-linked genes form long-range chromatin loops dependent on cohesin(39). Also, another study found that CTCF, especially when combined with YY1 or E2F2, promotes axon regeneration in peripheral neurons, suggesting that transcription factor cooperation and 3D chromatin architecture play key roles in activating regenerative gene programs(24). Notably, PATZ1 treatment led to an 11.6-fold increase in H3K27ac at growth-linked loci, likely priming these enhancers for productive enhancer-promoter interactions. This echoes a broader developmental pattern—embryonic and postnatal neurons, with high regenerative capacity, maintain more complex enhancer-promoter contacts than mature neurons. That structure is progressively lost with age. PATZ1's ability to activate enhancers while reshaping 3D chromatin organization positions it as a functional analog to cohesin in the context of regeneration. It may serve as a molecular bridge between local chromatin accessibility and the long-range regulatory interactions needed to unlock growth programs. These findings point to a fundamental principle: successful axon regeneration depends not only on turning on the right genes, but on reassembling the chromatin architecture that makes such activation possible.

In summary, we show that the transcription factor PATZ1 can reset adult corticospinal neurons to a juvenile, growth-ready state. During normal maturation, two post-natal "lock-down" waves progressively seal enhancers and promoters of axon-growth genes while PATZ1 binding fades. After thoracic injury, this restricted landscape permits only a modest, distance-limited chromatin response, but AAV-mediated PATZ1 delivery reverses the blockade: it expands injury-responsive accessible sites almost two-fold, boosts H3K27ac 11-fold at growth enhancers, triggers selective B → A compartment shifts, and sculpts smaller, growth-centric TADs. These architectural changes reactivate developmental growth programs and dampen apoptotic and inhibitory genes, yielding a potent, locus-specific epigenomic makeover without the off-target risks of broad chromatin drugs. The work identifies stripe-factor-guided remodeling as a tractable strategy to dismantle intrinsic epigenetic barriers and offers a blueprint for combining PATZ1 with classical pro-regenerative factors to drive functional CNS repair.

**Materials and Methods**

*Animal Husbandry:* All experimental protocols involving animals were approved by the Institutional Animal Ethics Committee (IAEC) of the Centre for Cellular and Molecular Biology (CCMB), Hyderabad, India (IAEC 14/2023, 29/2023, 51/2023, 10/2024, 53/2024). Mice were bred and maintained under a 24-hour light-dark cycle with 12 hours of light and 12 hours of darkness. The ambient temperature was maintained between 23-25°C with humidity levels between 40% and 60%.

*Cloning and Virus production:* Constructs for candidate genes were purchased from Horizon Discovery: pCMV-SPORT6-PATZ1 (Clone ID: 4167023) from the MGC Fully Sequenced Mouse cDNA (pCMV) Set Transcription Factors (Catalog ID: MMM5173, Expression Ready MGC cDNA Libraries), while pAAV-CAG-tdTomato (codon diversified) and pAAV-CAG-GFP were purchased from Addgene (Plasmid catalogue ID# 59462, #37825). For viral production, the ORF of each gene was cloned into an AAV-CAG backbone (Addgene Plasmid #59462) using a standard cut-and-paste method. Maxipreps were prepared using Qiagen Endo-free kits and fully sequenced. AAV9-tdTomato (Addgene Plasmid #59462) was produced in-house, achieving a titer value of 10×10^11 to 10^13 before injection. For experiments, viruses were mixed at a 1:3 ratio of pAAV-CAG-GFP to pAAV-CAG-PATZ1. List of plasmids used are available in Table 11.

*Animal Surgeries - Thoracic Crush:* Mice were anesthetized and prepared for surgery by shaving and disinfecting the upper back and neck. A midline incision was made from the ears to approximately 2 cm down the neck and back. Fatty tissue was displaced laterally, and a bulldog clamp was used to retract skin and maintain exposure of the surgical site. The underlying paraspinal musculature was carefully dissected to expose the spinal column. The spinous process at the T10-T12 level was identified and trimmed if necessary to facilitate access. The mouse was then mounted in a custom spine stabilizer to ensure proper immobilization during the procedure. A laminectomy was performed at the T10-T12 level using fine forceps to carefully remove the dorsal lamina and expose the spinal cord. The exposed spinal cord was then crushed with calibrated blunt forceps for a precise duration of 10 seconds, applying consistent pressure across the full width of the cord. Following crush injury, the vertebral column was repositioned, surrounding tissues were returned to their anatomical positions, and the skin was sutured with black nylon thread. Post-operative care included analgesics, antibiotics, manual bladder expression twice daily until function returned, and maintenance on a heating pad during recovery. Visible hindlimb paralysis was consistently observed post-surgery, confirming successful injury. All procedures were performed in a type II safety hood under aseptic conditions.

*Intra-cortical Surgery:* This procedure was modified from Wang *et al*.,2025(6). After deep anesthesia with ketamine/Xylazine, mice were prepared by shaving the scalp and neck and disinfecting with betadine. Mice were positioned in a stereotaxic frame, and a 1 cm midline incision was made in the scalp. The skin was retracted with a Bulldog clamp, and the skull over the injection area was gently

peeled away. Stereotaxic coordinates (x=-2, y=-0.5, z=+0.5, z= 0.6) were used to guide the procedure at specified points. A 30½ gauge needle bent into an L-shape, was inserted 0.6 mm from the brain surface and turned 90 degrees to sever axons. The needle was retracted, the skin was sutured, and post-operative care was provided.

*Anterograde Injections:* Following deep anesthesia with ketamine/Xylazine, mice were prepared by shaving and disinfecting the scalp and neck. They were positioned in a stereotaxic frame, and a 1 cm midline incision was made in the scalp. The skin was retracted with a Bulldog clamp, and a thin skull layer was gently peeled away. Non-replicating viral particles were injected using a Hamilton syringe at four bilateral points relative to Bregma, with coordinates (x = -2, +2; y = -1, -0.5, +0.5, +1, z= 0.8, 0.6), delivering 1 µl of AAV (0.2 µl/2 min) to ensure widespread diffusion. After withdrawal of the pipette, the incision was sutured and appropriate post-operative care was administered.

*Immunohistochemistry:* For spinal injury experiments, adult animals were decapitated following anesthesia, and the brain and spinal cord were extracted and post-fixed overnight in 4% PFA at 4°C. Spinal cord tissue was embedded in 12% gelatin (G2500-Sigma Aldrich) in PBS, and 50 µm sagittal sections were obtained using a vibratome. Sections were permeabilized in PBST, blocked with 5% normal goat serum, and incubated with anti-GFAP antibody (mAb #3670, Cell Signalling Technology, 1:500) overnight at 4°C. After washing, sections were incubated with Alexa Fluor-conjugated secondary antibodies (Thermo Fisher, 1:500) for 2 hours at room temperature. Following counterstaining with DAPI, sections were mounted and imaged using a STED microscope for high-resolution analysis.

*Nuclear extraction and Fluorescence-activated nuclei sorting (FANS):* Adult mice received anterograde injections of viral vectors for Control and PATZ1 treatment. One week later, animals were challenged with thoracic crush injuries, as described above. One week post-injury, animals were sacrificed, and the motor cortices were dissected. Tissue was collected only from the motor cortex region, which shows green fluorescence under UV light when viewed through a yellow filter. The dissected motor cortex tissues were added to pre-chilled 2ml EZ lysis buffer (Sigma, NUC-101) and dounced (Sigma, D9188) slowly and carefully (Dounce A, 40 times; Dounce B, 45 times), then incubated for 5 minutes at room temperature. Post incubation, the content was transferred to a 15ml falcon tube and centrifuged at 500g with acceleration and deceleration set to 2. The supernatant was removed, and the pellet was dissolved in Nuclear Suspension Buffer (freshly prepared: 5 mL PBS, 25 uL BSA (20 mg/mL) and 25 uL RNase inhibitor (40 U/uL)(Invitrogen, 10777019)) and strained through a Polystyrene tube with cell strainer (Falcon, 352235). Dissociated nuclei were flow-sorted on a BD FACS using an appropriate gating strategy (Sort type: Purity). Nuclei were first gated by side scatter height (SSC-H) vs. forward scatter height (FSC-H) and side scatter area (SSC-A) vs. FSC-A to separate debris from intact nuclei. Nuclei

that passed these filters were further selected by SSC-W vs. SSC-H to eliminate potential doublets. Finally, nuclei were gated by fluorescence marker intensity to collect only the brightest approximately 5000 nuclei for ATAC sequencing.

*Single Nuclear ATAC Sequencing Library construction (sn-ATAC):* Single-cell ATAC-seq datasets were generated using the Chromium Single Cell ATAC kit from 10x Genomics, following the manufacturer's instructions (10x Genomics, CG000496 Chromium Next GEM Single Cell ATAC Reagent Kit v2). Nuclei were isolated from the motor cortex of mice (n=3 per experimental group). The isolated nuclei suspensions (3,000-5,000 nuclei per sample) were added to the transposition mix containing Tn5 transposase enzyme, which simultaneously fragments DNA and inserts adapter sequences at accessible chromatin regions. Gel beads in emulsion (GEMs) were generated on the Chromium Next GEM Chip H by combining barcoded gel beads with the transposed nuclei suspension and partitioning oil. After GEM generation, the barcoded DNA fragments were recovered and purified using streptavidin beads, followed by size selection with SPRIselect beads (Beckman Coulter, B23318) and a series of 80% ethanol washes. The purified DNA fragments were eluted in elution buffer (10 mM Tris-HCl pH 8.0), followed by indexing PCR amplification (12 cycles) to add sample indices and Illumina sequencing adapters. Final library cleanup was performed using an additional round of size selection with SPRIselect beads. Library quality was assessed using a Bioanalyzer High Sensitivity DNA Kit (Agilent, 5067-4626) to confirm appropriate fragment size distribution (200-800 bp). Sequencing was performed on an Illumina NovaSeq 6000 instrument using a paired-end configuration with read length of 2X150 bp, approximately 300 million paired-end reads per sample to achieve sufficient coverage for downstream analysis.

*Bulk Assay for Transposase-Accessible Chromatin Sequencing:* Motor cortices were isolated from mouse pups at P0, P4, P7, and from adult mice that underwent intra-cortical and thoracic crush surgery. Tissue samples (20-30 mg) were minced and placed into ice-cold PBS. Nuclei extraction was performed following the protocol described above. Nuclei were counted, and approximately 50,000 to 100,000 nuclei per sample were used for the assay. The nuclear pellet was resuspended in Tagmentation Master Mix containing transposase enzyme (Active Motif, 53150), which inserts sequencing adapters into accessible regions of chromatin according to the manufacturer's protocol. Tagmentation was carried out by incubating the nuclei with the Tagmentation Master Mix at 37°C for 30 minutes with gentle agitation. Following tagmentation, the DNA was purified using a DNA purification column (Active Motif, included in kit). The purified DNA was eluted in 10 mM Tris-HCl (pH 8.0) and subjected to PCR amplification (12-15 cycles) using indexed primers compatible with Illumina sequencing. Post-PCR, a final purification step was performed using SPRI beads (Beckman Coulter, B23318) at a 1.8× ratio to remove primer dimers and unincorporated primers. Libraries were quantified using Qubit dsDNA HS Assay Kit (Thermo Fisher, Q32851), and DNA size distribution was assessed with a TapeStation 4200

(Agilent) using a D1000 ScreenTape (Agilent, 5067-5582) before pooling and loading the libraries onto the Illumina NovaSeq 6000 sequencing platform for ~30 million paired-end reads per library.

*High throughput Chromosome Confirmation Capture (Hi-C):* Mice used for the assay were subjected to anterograde injections of AAV9-PATZ1, followed by a thoracic crush injury one week later. Hi-C was performed on two types of tissues: mice at 7 days post-injury, and injured mice injected with AAV9-PATZ1, with the protocol individually performed for each tissue type. Hi-C was carried out following the in situ Hi-C protocol provided by the ENCODE Consortium. Briefly, the motor cortices (35-40mg, from 3 to 5 animals) were isolated from the mouse brain, and the tissues were crosslinked with 1% formaldehyde (Thermofisher, 12755) for 10 minutes at room temperature. After quenching with 2.5M glycine solution (MP Biomedicals, 808822) to a final concentration of 0.2M for 5 minutes, nuclei were isolated through cell lysis using cold Hi-C lysis buffer (5mM CaCl2, 3mM MgAc, 2mM EDTA, 0.5mM EGTA, 10mM Tris-HCl pH8.0, 1mM DTT, 0.1mM PMSF) with protease inhibitors (MCE, HY-K0010). After density gradient centrifugation with 1M Sucrose solution, nuclei were resuspended in 0.5% SDS and incubated at 62°C for 10 minutes. SDS was quenched with 10% Triton X-100, and chromatin was digested with 100U of MboI restriction enzyme (NEB, R0147) at 37°C overnight. Following enzyme inactivation at 62°C for 20 minutes, DNA ends were filled in with a mix containing biotin-14-dATP (0.4mM) (Thermo Scientific, 19524-016), dCTP, dGTP, dTTP (10mM each) (Thermo Scientific, 18254011, 18253013, 18255018) and DNA Polymerase I Klenow Fragment (NEB, M0210) at 37°C for 45 minutes. Ligation was performed in a master mix containing T4 DNA ligase buffer, 10% Triton X-100, 20mg/ml BSA (Catalog no :A7906-Sigma), and T4 DNA Ligase (NEB, M0202) at room temperature for 4 hours. After proteinase K (Sigma, P2308) treatment and crosslink reversal at 65°C overnight, DNA was purified, sheared using Covaris (M220, Condition Peak Incident: 50, Duty Factor= 10, Cycles/Burst=350, Treatment Time= 70), and size-selected for 300-500bp fragments using AMPure XP beads (Beckman Coulter, A63881). Biotin-labeled fragments were captured with Streptavidin T1 beads (Invitrogen, 65601), end-repaired, dA-tailed, and ligated to Illumina adapters (Illumina TruSeq UD Indexes, 20040870). The final library was PCR amplified (Illumina, 20015964), purified again with AMPure XP beads, and sequenced to a depth of ~500 million paired-end reads on the Illumina NovaSeq platform.

*Cleavage Under Targets and Release Using Nuclease Sequencing (CUT&RUN):* Mice received anterograde intracortical injections of AAV9-PATZ1, followed by thoracic spinal cord injury seven days later. CUT&RUN was performed using the DNA-Protein Interaction Assay Kit (Cell Signalling Technology, #86652) according to the manufacturer's protocol. Motor cortices were dissected and fixed with 0.1% formaldehyde (Cell Signalling Technology, #12606P), then quenched using 10x glycine (Cell Signalling Technology, #7005S). Tissue was dissociated into cell suspensions using a Dounce homogenizer in wash buffer containing spermidine (Cell Signalling Technology, #27287) and protease

inhibitors (Cell Signalling Technology, #7012). Cells were bound to activated Concanavalin A beads and incubated overnight at 4°C with the PATZ1 antibody (MyBioSource, MSB9403528).
The following day, pAG-MNase enzyme was added in a buffer premix (Cell Signalling Technology, #15338) containing digitonin (Cell Signalling Technology, #16359), spermidine, and protease inhibitors, and incubated with the sample for 1 hour. DNA cleavage was activated on ice by adding $CaCl_2$ in a digitonin-containing buffer and incubating at 4°C for 30 minutes. DNA fragments were released by adding Stop Buffer (Cell Signalling Technology, #48105) containing digitonin and RNase A (Cell Signalling Technology, #7013), followed by a 10-minute incubation at 37°C. Crosslinks were reversed using 10% SDS and 20 mg/mL Proteinase K (Cell Signalling Technology, #10012), with incubation at 65°C for 2 hours. DNA was purified using DNA Purification Buffers and Spin Columns (Cell Signalling Technology, #14209) following the manufacturer's recommended protocol. Libraries were prepared by end repair, adaptor ligation, and PCR amplification using the NEBNext® Ultra™ II DNA Library Prep Kit (NEB, #E7103).
Input samples were prepared using a similar protocol, except they were not treated with antibody or pAG-MNase. Instead, DNA was extracted using DNA Extraction Buffer (Cell Signalling Technology, #42015) for sonication (Covaris M220; 100–600 bp, Peak Incident: 75, Duty: 10, Cycles/Burst: 200, 75 s), followed by library preparation. Both CUT&RUN and input libraries were sequenced to 5 million paired-end reads (Illumina NovaSeq).
Additionally, motor cortices were isolated from uninjured mice, mice 7 days post-injury, and mice treated with AAV-PATZ1 prior to thoracic injury. CUT&RUN assays were performed using the H3K27ac antibody (Abcam, ab4729) and CTCF antibody (Cell Signalling Technology, #3418), following the manufacturer's protocol outlined above. These libraries were then amplified and sequenced to a depth of 5 million paired-end reads.

*Single nuclei RNA Sequencing:* Single-nuclei RNA sequencing (snRNA-seq) was performed using the Chromium Next GEM Single Cell 3' v3.1 (Dual Index) platform (10x Genomics) following the manufacturer's protocol (Document CG000315 Rev F). Nuclei were isolated from the motor cortex of mice (n=3 per sample) injected with AAV-GFP (control) and AAV-PATZ1 according to the nuclei isolation procedure mentioned above. It was then FACS sorted to isolate only GFP AND DAPI positive nuclei population. The cell suspensions were loaded onto the Chromium Next GEM Chip G (PN-2000177) for generating Gel Beads-in-Emulsion (GEM). Single cell suspensions were combined with Master Mix containing RT Reagent B (PN-2000165), Template Switch Oligo (PN-3000228), Reducing Agent B (PN-2000087), and RT Enzyme C (PN-2000085/2000102). A total of approximately 4000 cells were targeted. Cell suspensions and Master Mix were loaded into the Chromium Next GEM Chip G along with Single Cell 3' v3.1 Gel Beads (PN-2000164) and Partitioning Oil (PN-2000190).
The chip was processed on the Chromium Controller to generate GEMs. Within each GEM, cells were lysed, and mRNAs were captured by poly(dT) oligonucleotides attached to the gel beads, which also

contained a 16-nucleotide 10x Barcode, a 12-nucleotide Unique Molecular Identifier (UMI), and adaptor sequences. Reverse transcription was performed within the GEMs using the following thermal cycling protocol: 53°C for 45 minutes, followed by 85°C for 5 minutes. Following reverse transcription, GEMs were broken using Recovery Agent (PN-220016), and the barcoded, full-length cDNA was purified using Dynabeads MyOne SILANE (PN-2000048). Cleanup Buffer (PN-2000088) and Reducing Agent B (PN-2000087) were used in the Dynabeads Cleanup Mix. The purified cDNA was amplified using cdna Primers (PN-2000089) and Amp Mix (PN-2000047/2000103) with the following cycling parameters mentioned in the protocol. The number of PCR cycles was optimised based on the targeted cell recovery, with 12 cycles used for 500-6,000 cells. Amplified cDNA was cleaned up using SPRIselect reagent (Beckman Coulter, PN B23318) at a ratio of 0.6X, and the purified cDNA was quality-checked and quantified using the Agilent Tapestation 4200 using D1000 tape (PN-5067-5586).
For library construction, 25% of the total cDNA yield was used as input. The cDNA was enzymatically fragmented using Fragmentation Enzyme (PN-2000090/2000104) and Fragmentation Buffer (PN-2000091), followed by end-repair and A-tailing. The fragmentation reaction was incubated at 32°C for 5 minutes, followed by 65°C for 30 minutes. Size selection was performed using SPRIselect reagent with a double-sided protocol (0.6x followed by 0.8x) to obtain fragments of optimal size. Adaptor ligation was performed using Ligation Buffer (PN-2000092), DNA Ligase (PN-220110/220131), and Adaptor Oligos (PN-2000094) at 20°C for 15 minutes. After another round of cleanup using SPRIselect (0.8x), Sample Index PCR was performed using Amp Mix (PN-2000047/2000103) and dual indices from the Dual Index Kit TT Set A (PN-1000215, containing index plate PN-3000431). PCR cycling conditions were: 98°C for 45 seconds, followed by 12 cycles of (98°C for 20 seconds, 54°C for 30 seconds, 72°C for 20 seconds), with a final extension at 72°C for 1 minute. The final libraries were purified using a double-sided size selection with SPRIselect (0.6x followed by 0.8x) to remove adapter dimers and were eluted in Buffer EB (Qiagen, PN-19086).
Libraries were quality-checked using an Agilent Tapestation with D1000 tape to verify fragment size distribution (~200-2,000 bp with a peak around 400 bp). Libraries were sequenced on an Illumina NovaSeq 6000 sequencer with a depth of 300 million paired-end reads.

*Adeno-Associated Virus Production:* Adeno-associated viral (AAV) particles, serotype 9, were packaged and produced in HEK293T cells and then purified using a commercial AAV purification kit (Takara, Catalog#6675). Briefly, HEK293T cells were transiently transfected with pAAV-CAG-Patz1, pAAV2/9n (Addgene, Catalog#112865), and pAdDeltaF6 (Addgene, Catalog#112867) using Transfection Grade Linear Polyethylenimine Hydrochloride (MW 40,000) (Polysciences, Catalog#24765). At 48 hours post-transfection, cells were dislodged and transferred to sterile 50 ml falcon tubes. Viral isolation was performed following the manufacturer's instructions.To assess AAV capsid formation, proteins were separated on a 10% SDS-PAGE gel at 35 mA for 120 minutes. The gel was stained with Coomassie Brilliant Blue (Himedia, Catalog#17524.02) for 20 minutes, followed by

overnight destaining in a solution of 10% acetic acid (Himedia, Catalog#90868) and 40% methanol (Himedia, Catalog#AS059) in water. SDS-PAGE analysis confirmed the presence of all three AAV capsid proteins: VP1 (83kDa), VP2 (73kDa), and VP3 (62kDa), with VP3 being the most abundant as expected for correctly assembled AAV particles.For viral titer quantification, qPCR was performed using the Takara TB Green Premix Ex Taq II kit (Takara, Catalog#RR82WR). Viral particles were first treated with DNase for 30 minutes at 37°C, then serially diluted ten-fold across four dilutions. The viral titer was estimated by comparing the Ct values of the viral particles with known plasmid standard (Addgene Plasmid #59462) from a standard curve. All AAV preparations yielded titers of 10^11 viral genomes per ml or higher, with intact capsid formation confirmed by SDS-PAGE analysis.

*Single Nuclear ATAC Sequencing Analysis Pipeline:* Cell Ranger ATAC was used to process Chromium scATAC-seq data following protocols described previously(46). Fragment files were imported into ArchR version 1.0.2(47). We applied stringent quality control filters, retaining only cells with >1,000 fragments and >4 transcription start site (TSS) enrichment score. After quality control and filtering of empty droplets and doublets, we identified approximately 72,000 peaks from 1,500 nuclei per sample. Gene activities for each nucleus were calculated using the GeneScoreMatrix() function by summing peak counts in the gene body plus 2 kilobase pairs (kb) upstream(40). Data were normalized using term frequency-inverse document frequency (TF-IDF) normalization (RunTFIDF), followed by dimensionality reduction using singular value decomposition (RunSVD). K-nearest neighbors were calculated using FindNeighbours (reduction = "lsi", dims = 2:30). Cell clusters were identified using a shared nearest neighbor (SNN) modularity optimization-based clustering algorithm FindClusters (algorithm = 3, resolution = 2). UMAP visualization was generated using the RunUMAP function with reduction = "lsi" and dims = 2:30. Peaks were called using the addReproduciblePeakSet() function in ArchR using the Tiles matrix method with a fixed width of 501 base pairs. The complete automated analysis workflow is documented in detail on our GitHub repository https://github.com/VenkateshLab/Targeted-chromatin-remodeling-by-PATZ1.

*Bulk ATAC Sequencing Analysis Pipeline:* Mouse forebrain samples were collected from the ENCODE project at various developmental stages, including embryonic days E11, E12, E13, E14, and E18, as well as postnatal stages P0 and adult. Additional Bulk ATAC-seq datasets were generated for other developmental stages as described above. Paired-end reads were trimmed using fastp to remove adapter sequences and low-quality bases(48). Trimmed reads were aligned to the mouse genome (mm10) using the STAR aligner with default parameters(49). We filtered out reads with mapping quality scores lower than 10 using SAMtools and removed duplicate reads using the MarkDuplicates function from the Picard toolkit (50). For downstream analysis, we employed the TOBIAS-snake pipeline with default parameters (51). BigWig files were generated for visualization in the UCSC Genome Browser(52). The complete automated pipeline details are available in our GitHub repository https://github.com/VenkateshLab/Targeted-chromatin-remodeling-by-PATZ1.

*CUT&RUN Analysis Pipeline:* Raw sequencing reads were processed with FastP for adapter removal and low-quality read trimming. Clean reads were aligned to the mouse genome (mm10) using BWA-mem with default parameters(50). Aligned reads were converted to BAM format and sorted using SAMtools, and PCR duplicates were removed with Picard. Peak calling was performed using MACS2 with default parameters(53). Identified peaks were annotated using GenomicRanges and ChIPseeker packages in R(54). The annotated BED files were further analyzed to identify CTCF binding sites and enhancer regions using resources from the SCREEN project from ENCODE(40). The complete automated analysis workflow is documented in detail on our GitHub repository mentioned above.

*snRNA-seq Data Analysis Pipeline*: Our workflow began with raw data quality assessment using FastQC ensuring sequencing data met basic quality thresholds for base quality, adapter contamination, and overall read quality. Following quality assessment, we used FastP to remove low-quality reads, filtering out those with poor quality scores or excessive adapter sequences (48). The cleaned data was processed using CellRanger, which was specifically designed for single-nucleus RNA-seq data alignment and quantification(55). We used the mm10 mouse reference genome with default parameters to generate high-quality alignments. Samples were sequenced to an average depth of ~70,000 reads/nucleus (3,000-4,000 nuclei per library) on an Illumina NovaSeq platform.
The datasets were integrated using SEURAT v5 (56)and differential expression analysis was conducted using the "FindMarkers" function, applying a nonparametric Wilcoxon rank-sum test. Cluster visualization in Seurat was generated using the "scCustomize" package in R (https://github.com/samuel-marsh/scCustomize), while MA-plots, histograms, and heatmaps were created using the "ggplot2" package (https://ggplot2.tidyverse.org/). We utilized ShinyCell in R to provide pre-built clusters of the analyzed scRNA-seq data, enabling direct visualization and interactive exploration (57). The clustered data is publicly accessible through our dedicated webpage.
*Hi-C Data Processing and 3D Genome Architecture Analysis:* Paired-end Hi-C sequencing reads were initially subjected to quality control using FastQC (v0.11.9) to assess base quality, GC content, and adapter contamination (58). Trimming of 3′ overhangs was performed using homerTools (v4.11), specifically targeting the MboI/DpnII restriction enzyme motif (GATC), with parameters -mis 0, -matchStart 20, and -min 20. Both R1 and R2 reads were trimmed independently, as paired-end alignment is not recommended for HOMER Hi-C analysis.Trimmed reads were aligned to the Mus musculus mm10 reference genome using Bowtie2 (v2.5.1) with the -U flag for unpaired alignment and -p 30 for parallel processing. The resulting SAM files were used to generate a Hi-C tag directory via HOMER's makeTagDirectory function, using the -tbp 1 option to remove PCR duplicates. Additional QC metrics were generated using parameters such as -checkGC, -restrictionSite GATC, and -genome mm10. For interactive visualization in Juicebox, .hic files were generated using HOMER's tagDir2hicFile.pl utility (59)

*Chromatin Compartment Analysis (PCA):* Principal component analysis (PCA) was performed using the runHiCpca.pl script to identify chromatin compartments (A/B) at a resolution of 25 kb with a 50 kb smoothing window. This analysis generated both .PC1.bedGraph and .PC1.txt files, where the PC1 values correlate with open (A) and closed (B) chromatin domains. The bedGraph files were visualized in a genome browser and used for comparative analysis between control and treated samples. Control vs. treated conditions were integrated using annotatePeaks.pl, and differentially enriched compartments were identified using getDiffExpression.pl, with group labels specified according to replicate structure.
*Chromatin Compaction Analysis:* Chromatin compaction was quantified using distal-to-local interaction ratios (DLR) and interchromosomal interaction fractions (ICF) via the analyzeHiC function with -compactionStats parameter. This analysis was performed at 5 kb resolution with a 15 kb window. Output .DLR.bedGraph and .ICF.bedGraph files were processed using subtractBedGraphs.pl to identify differential compaction profiles across conditions.
*TAD and Loop Detection:* Topologically associating domains (TADs) and chromatin loops were detected using findTADsAndLoops.pl with a 3 kb resolution and a 15 kb window size. The resulting .loop.2D.bed and .tad.2D.bed files were visualized using Juicebox and served as the basis for cross-condition comparisons. To compare loop and TAD dynamics between control and treated samples, feature files were first merged using merge2Dbed.pl. Quantification was performed using findTADsAndLoops.pl score across all tag directories. Differential enrichment analysis was conducted using getDiffExpression.pl, identifying significantly altered loops and TADs between conditions via an edgeR-based statistical framework (60).

*Acknowledgements*
We thank CSIR-CCMB for providing research facilities and support staff. We acknowledge Mrs. Zareena Begum (Tissue Culture), Mr. S. Prasanth and Mr. N. Sai Ram (Animal House), Dr. Karthik Baradwaj, Ms. Tulasi Nagabandi, and Dr. Md. Jafurulla (Genomics), Mr. G. Srinivas (FACS), and Mr. B. Suman and Dr. Nitla Venkata Mahesh (Microscopy) for their technical assistance. We also appreciate Fine Bio Chemical for the timely chemical supplies. This research was supported by funding from CSIR (HCP53201), DBT (BT/PR51467/MED/122/358/2024), and SERB (SRG00116).

*Data and code availability*: All genomics datasets generated in this study have been deposited in the NCBI Gene Expression Omnibus (GEO) under accession number **PRJNA1217518**. A detailed summary of datasets and corresponding sample information is provided in **Table 11**. The metadata detailing the tables used for the results is provided in **Table 12**. The code used for data processing and figure generation is available at https://github.com/VenkateshLab/Targeted-chromatin-remodeling-by-PATZ1. Additionally, all datasets have been integrated into an interactive, user-friendly web interface accessible at https://patz1.netlify.app/ to facilitate data exploration.

**References**


1. Venkatesh,I. and Blackmore,M.G. (2017) Selecting optimal combinations of transcription factors to promote axon regeneration: Why mechanisms matter. *Neurosci Lett*, **652**, 64–73.

2. Sun,F. and He,Z. (2010) Neuronal intrinsic barriers for axon regeneration in the adult CNS. *Curr Opin Neurobiol*, **20**, 510–518.

3. Mahar,M. and Cavalli,V. (2018) Intrinsic mechanisms of neuronal axon regeneration. *Nat Rev Neurosci*, **19**, 323–337.

4. Wang,Z., Mehra,V., Simpson,M.T., Maunze,B., Chakraborty,A., Holan,L., Eastwood,E., Blackmore,M.G. and Venkatesh,I. (2018) KLF6 and STAT3 co-occupy regulatory DNA and functionally synergize to promote axon growth in CNS neurons. *Sci Rep*, **8**, 12565.

5. Blackmore,M.G. (2012) Molecular control of axon growth: insights from comparative gene profiling and high-throughput screening. *Int Rev Neurobiol*, **105**, 39–70.

6. Wang,Z., Kumaran,M., Batsel,E., Testor-Cabrera,S., Beine,Z., Alvarez Ribelles,A., Tsoulfas,P., Venkatesh,I. and Blackmore,M.G. (2025) Single-nuclei sequencing reveals a robust corticospinal response to nearby axotomy but overall insensitivity to spinal injury. *J. Neurosci.*, 10.1523/JNEUROSCI.1508-24.2024.

7. Moore,D.L., Blackmore,M.G., Hu,Y., Kaestner,K.H., Bixby,J.L., Lemmon,V.P. and Goldberg,J.L. (2009) KLF family members regulate intrinsic axon regeneration ability. *Science*, **326**, 298–301.

8. Jacobi,A., Tran,N.M., Yan,W., Benhar,I., Tian,F., Schaffer,R., He,Z. and Sanes,J.R. (2022) Overlapping transcriptional programs promote survival and axonal regeneration of injured retinal ganglion cells. *Neuron*, **110**, 2625-2645.e7.

9. Sun,F., Park,K.K., Belin,S., Wang,D., Lu,T., Chen,G., Zhang,K., Yeung,C., Feng,G., Yankner,B.A., *et al.* (2011) Sustained axon regeneration induced by co-deletion of PTEN and SOCS3. *Nature*, **480**, 372–375.

10. Shin,J.E., Cho,Y., Beirowski,B., Milbrandt,J., Cavalli,V. and DiAntonio,A. (2012) Dual Leucine Zipper Kinase Is Required for Retrograde Injury Signaling and Axonal Regeneration. *Neuron*, **74**, 1015–1022.

11. Yiu,G. and He,Z. (2006) Glial inhibition of CNS axon regeneration. *Nat Rev Neurosci*, **7**, 617–627.

12. Fawcett,J.W. and Asher,R.A. (1999) The glial scar and central nervous system repair. *Brain Res Bull*, **49**, 377–391.

13. Venkatesh,I., Mehra,V., Wang,Z., Califf,B. and Blackmore,M.G. (2018) Developmental Chromatin Restriction of Pro-Growth Gene Networks Acts as an Epigenetic Barrier to Axon Regeneration in Cortical Neurons. *Dev Neurobiol*, **78**, 960–977.

14. Venkatesh,I., Simpson,M.T., Coley,D.M. and Blackmore,M.G. (2016) Epigenetic profiling reveals a developmental decrease in promoter accessibility during cortical maturation in vivo. *Neuroepigenetics*, **8**, 19–26.

15. Blackmore,M.G. (2012) Molecular control of axon growth: insights from comparative gene profiling and high-throughput screening. *Int Rev Neurobiol*, **105**, 39–70.

16. Blackmore,M.G., Moore,D.L., Smith,R.P., Goldberg,J.L., Bixby,J.L. and Lemmon,V.P. (2010) High content screening of cortical neurons identifies novel regulators of axon growth. *Mol Cell Neurosci*, **44**, 43–54.

17. Moore,D.L., Blackmore,M.G., Hu,Y., Kaestner,K.H., Bixby,J.L., Lemmon,V.P. and Goldberg,J.L. (2009) KLF family members regulate intrinsic axon regeneration ability. *Science*, **326**, 298–301.

18. Seijffers,R., Mills,C.D. and Woolf,C.J. (2007) ATF3 Increases the Intrinsic Growth State of DRG Neurons to Enhance Peripheral Nerve Regeneration. *J. Neurosci.*, **27**, 7911–7920.

19. Simpson,M.T., Venkatesh,I., Callif,B.L., Thiel,L.K., Coley,D.M., Winsor,K.N., Wang,Z., Kramer,A.A., Lerch,J.K. and Blackmore,M.G. (2015) The tumor suppressor HHEX inhibits axon growth when prematurely expressed in developing central nervous system neurons. *Mol Cell Neurosci*, **68**, 272–283.

20. Williams,R.R., Venkatesh,I., Pearse,D.D., Udvadia,A.J. and Bunge,M.B. (2015) MASH1/Ascl1a leads to GAP43 expression and axon regeneration in the adult CNS. *PLoS One*, **10**, e0118918.

21. Dhara,S.P., Rau,A., Flister,M.J., Recka,N.M., Laiosa,M.D., Auer,P.L. and Udvadia,A.J. (2019) Cellular reprogramming for successful CNS axon regeneration is driven by a temporally changing cast of transcription factors. *Sci Rep*, **9**, 14198.

22. Venkatesh,I., Mehra,V., Wang,Z., Simpson,M.T., Eastwood,E., Chakraborty,A., Beine,Z., Gross,D., Cabahug,M., Olson,G., *et al.* (2021) Co-occupancy identifies transcription factor co-operation for axon growth. *Nat Commun*, **12**, 2555.

23. Chandran,V., Coppola,G., Nawabi,H., Omura,T., Versano,R., Huebner,E.A., Zhang,A., Costigan,M., Yekkirala,A., Barrett,L., *et al.* (2016) A Systems-Level Analysis of the Peripheral Nerve Intrinsic Axonal Growth Program. *Neuron*, **89**, 956–970.

24. Avraham,O., Le,J., Leahy,K., Li,T., Zhao,G. and Cavalli,V. (2022) Analysis of neuronal injury transcriptional response identifies CTCF and YY1 as co-operating factors regulating axon regeneration. *Front Mol Neurosci*, **15**, 967472.

25. Bareyre,F.M., Garzorz,N., Lang,C., Misgeld,T., Büning,H. and Kerschensteiner,M. (2011) In vivo imaging reveals a phase-specific role of STAT3 during central and peripheral nervous system axon regeneration. *Proc. Natl. Acad. Sci. U.S.A.*, **108**, 6282–6287.

26. Mehta,S.T., Luo,X., Park,K.K., Bixby,J.L. and Lemmon,V.P. (2016) Hyperactivated Stat3 boosts axon regeneration in the CNS. *Experimental Neurology*, **280**, 115–120.

27. Li,S., Xue,C., Yuan,Y., Zhang,R., Wang,Y., Wang,Y., Yu,B., Liu,J., Ding,F., Yang,Y., *et al.* (2015) The transcriptional landscape of dorsal root ganglia after sciatic nerve transection. *Sci Rep*, **5**, 16888.

28. Raivich,G., Bohatschek,M., Costa,C.D., Iwata,O., Galiano,M., Hristova,M., Nateri,A.S., Makwana,M., Riera-Sans,L., Wolfer,D.P., *et al.* (2004) The AP-1 Transcription Factor c-Jun Is Required for Efficient Axonal Regeneration. *Neuron*, **43**, 57–67.

29. Tian,F., Cheng,Y., Zhou,S., Wang,Q., Monavarfeshani,A., Gao,K., Jiang,W., Kawaguchi,R., Wang,Q., Tang,M., *et al.* (2022) Core transcription programs controlling injury-induced neurodegeneration of retinal ganglion cells. *Neuron*, **110**, 2607-2624.e8.

30. Trakhtenberg,E.F. and Goldberg,J.L. (2012) Epigenetic regulation of axon and dendrite growth. *Front. Mol. Neurosci.*, **5**.

31. Finelli,M.J., Wong,J.K. and Zou,H. (2013) Epigenetic Regulation of Sensory Axon Regeneration after Spinal Cord Injury. *J. Neurosci.*, **33**, 19664–19676.

32. VandenBosch,L.S. and Reh,T.A. (2020) Epigenetics in neuronal regeneration. *Seminars in Cell & Developmental Biology*, **97**, 63–73.

33. Puttagunta,R., Tedeschi,A., Sória,M.G., Hervera,A., Lindner,R., Rathore,K.I., Gaub,P., Joshi,Y., Nguyen,T., Schmandke,A., *et al.* (2014) PCAF-dependent epigenetic changes promote axonal regeneration in the central nervous system. *Nat Commun*, **5**, 3527.

34. Gaub,P., Tedeschi,A., Puttagunta,R., Nguyen,T., Schmandke,A. and Di Giovanni,S. (2010) HDAC inhibition promotes neuronal outgrowth and counteracts growth cone collapse through CBP/p300 and P/CAF-dependent p53 acetylation. *Cell Death Differ*, **17**, 1392–1408.

35. Gaub,P., Joshi,Y., Wuttke,A., Naumann,U., Schnichels,S., Heiduschka,P. and Di Giovanni,S. (2011) The histone acetyltransferase p300 promotes intrinsic axonal regeneration. *Brain*, **134**, 2134–2148.

36. Tedeschi,A., Nguyen,T., Puttagunta,R., Gaub,P. and Di Giovanni,S. (2009) A p53-CBP/p300 transcription module is required for GAP-43 expression, axon outgrowth, and regeneration. *Cell Death Differ*, **16**, 543–554.

37. Weng,Y.-L., An,R., Cassin,J., Joseph,J., Mi,R., Wang,C., Zhong,C., Jin,S.-G., Pfeifer,G.P., Bellacosa,A., *et al.* (2017) An Intrinsic Epigenetic Barrier for Functional Axon Regeneration. *Neuron*, **94**, 337-346.e6.

38. Palmisano,I., Danzi,M.C., Hutson,T.H., Zhou,L., McLachlan,E., Serger,E., Shkura,K., Srivastava,P.K., Hervera,A., Neill,N.O., *et al.* (2019) Epigenomic signatures underpin the axonal regenerative ability of dorsal root ganglia sensory neurons. *Nat Neurosci*, **22**, 1913–1924.

39. Palmisano,I., Liu,T., Gao,W., Zhou,L., Merkenschlager,M., Mueller,F., Chadwick,J., Toscano Rivalta,R., Kong,G., King,J.W.D., *et al.* (2024) Three-dimensional

chromatin mapping of sensory neurons reveals that promoter–enhancer looping is required for axonal regeneration. *Proc. Natl. Acad. Sci. U.S.A.*, **121**, e2402518121.

40. The ENCODE Project Consortium, Abascal,F., Acosta,R., Addleman,N.J., Adrian,J., Afzal,V., Ai,R., Aken,B., Akiyama,J.A., Jammal,O.A., *et al.* (2020) Expanded encyclopaedias of DNA elements in the human and mouse genomes. *Nature*, **583**, 699–710.

41. Zhao,Y., Vartak,S.V., Conte,A., Wang,X., Garcia,D.A., Stevens,E., Kyoung Jung,S., Kieffer-Kwon,K.-R., Vian,L., Stodola,T., *et al.* (2022) "Stripe" transcription factors provide accessibility to co-binding partners in mammalian genomes. *Molecular Cell*, **82**, 3398-3411.e11.

42. Ma,H., Ow,J.R., Tan,B.C.P., Goh,Z., Feng,B., Loh,Y.H., Fedele,M., Li,H. and Wu,Q. (2014) The dosage of Patz1 modulates reprogramming process. *Sci Rep*, **4**, 7519.

43. Mancinelli,S., Vitiello,M., Donnini,M., Mantile,F., Palma,G., Luciano,A., Arra,C., Cerchia,L., Liguori,G.L. and Fedele,M. (2021) The Transcription Regulator Patz1 Is Essential for Neural Stem Cell Maintenance and Proliferation. *Front. Cell Dev. Biol.*, **9**, 657149.

44. Ow,J.R., Ma,H., Jean,A., Goh,Z., Lee,Y.H., Chong,Y.M., Soong,R., Fu,X.-Y., Yang,H. and Wu,Q. (2014) Patz1 Regulates Embryonic Stem Cell Identity. *Stem Cells and Development*, **23**, 1062–1073.

45. Valentino,T., Palmieri,D., Vitiello,M., Simeone,A., Palma,G., Arra,C., Chieffi,P., Chiariotti,L., Fusco,A. and Fedele,M. (2013) Embryonic defects and growth alteration in mice with homozygous disruption of the *Patz1* gene. *Journal Cellular Physiology*, **228**, 646–653.

46. Satpathy,A.T., Granja,J.M., Yost,K.E., Qi,Y., Meschi,F., McDermott,G.P., Olsen,B.N., Mumbach,M.R., Pierce,S.E., Corces,M.R., *et al.* (2019) Massively parallel single-cell chromatin landscapes of human immune cell development and intratumoral T cell exhaustion. *Nat Biotechnol*, **37**, 925–936.

47. Granja,J.M., Corces,M.R., Pierce,S.E., Bagdatli,S.T., Choudhry,H., Chang,H.Y. and Greenleaf,W.J. (2021) ArchR is a scalable software package for integrative single-cell chromatin accessibility analysis. *Nat Genet*, **53**, 403–411.

48. Chen,S., Zhou,Y., Chen,Y. and Gu,J. (2018) fastp: an ultra-fast all-in-one FASTQ preprocessor. *Bioinformatics*, **34**, i884–i890.

49. Dobin,A., Davis,C.A., Schlesinger,F., Drenkow,J., Zaleski,C., Jha,S., Batut,P., Chaisson,M. and Gingeras,T.R. (2013) STAR: ultrafast universal RNA-seq aligner. *Bioinformatics*, **29**, 15–21.

50. Li,H., Handsaker,B., Wysoker,A., Fennell,T., Ruan,J., Homer,N., Marth,G., Abecasis,G., Durbin,R., and 1000 Genome Project Data Processing Subgroup (2009) The Sequence Alignment/Map format and SAMtools. *Bioinformatics*, **25**, 2078–2079.

51. Bentsen,M., Goymann,P., Schultheis,H., Klee,K., Petrova,A., Wiegandt,R., Fust,A., Preussner,J., Kuenne,C., Braun,T., *et al.* (2020) ATAC-seq footprinting unravels

kinetics of transcription factor binding during zygotic genome activation. *Nat Commun*, **11**, 4267.

52. Raney,B.J., Barber,G.P., Benet-Pagès,A., Casper,J., Clawson,H., Cline,M.S., Diekhans,M., Fischer,C., Navarro Gonzalez,J., Hickey,G., *et al.* (2024) The UCSC Genome Browser database: 2024 update. *Nucleic Acids Research*, **52**, D1082–D1088.

53. Zhang,Y., Liu,T., Meyer,C.A., Eeckhoute,J., Johnson,D.S., Bernstein,B.E., Nusbaum,C., Myers,R.M., Brown,M., Li,W., *et al.* (2008) Model-based Analysis of ChIP-Seq (MACS). *Genome Biol*, **9**, R137.

54. Yu,G., Wang,L.-G. and He,Q.-Y. (2015) ChIPseeker: an R/Bioconductor package for ChIP peak annotation, comparison and visualization. *Bioinformatics*, **31**, 2382–2383.

55. Zheng,G.X.Y., Terry,J.M., Belgrader,P., Ryvkin,P., Bent,Z.W., Wilson,R., Ziraldo,S.B., Wheeler,T.D., McDermott,G.P., Zhu,J., *et al.* (2017) Massively parallel digital transcriptional profiling of single cells. *Nat Commun*, **8**, 14049.

56. Butler,A., Hoffman,P., Smibert,P., Papalexi,E. and Satija,R. (2018) Integrating single-cell transcriptomic data across different conditions, technologies, and species. *Nat Biotechnol*, **36**, 411–420.

57. Ouyang,J.F., Kamaraj,U.S., Cao,E.Y. and Rackham,O.J.L. (2021) ShinyCell: simple and sharable visualization of single-cell gene expression data. *Bioinformatics*, **37**, 3374–3376.

58. Brown,J., Pirrung,M. and McCue,L.A. (2017) FQC Dashboard: integrates FastQC results into a web-based, interactive, and extensible FASTQ quality control tool. *Bioinformatics*, **33**, 3137–3139.

59. Durand,N.C., Robinson,J.T., Shamim,M.S., Machol,I., Mesirov,J.P., Lander,E.S. and Aiden,E.L. (2016) Juicebox Provides a Visualization System for Hi-C Contact Maps with Unlimited Zoom. *Cell Syst*, **3**, 99–101.

60. Robinson,M.D., McCarthy,D.J. and Smyth,G.K. (2010) edgeR : a Bioconductor package for differential expression analysis of digital gene expression data. *Bioinformatics*, **26**, 139–140.